# Void growth yield criteria for intergranular ductile fracture

Cedric Senac, Jeremy Hure, Benoît Tanguy

# Void growth yield criteria for intergranular ductile fracture

C. Sénac[a,*], J. Hure[a], B. Tanguy[a]

[a] *Université Paris-Saclay, CEA, Service d'Étude des Matériaux Irradiés, 91191, Gif-sur-Yvette, France*

**Abstract**

Ductile fracture through growth and coalescence of intergranular cavities is a failure mode observed experimentally in many metallic alloys used in industrial applications. Simulation of this fracture process in polycristalline aggregates requires modeling of the plastic yielding of porous boundaries. However, classical yield criteria for porous materials such as the Gurson–Tvergaard–Needleman model and its current extensions cannot account for the complex coupling between loading state, crystallographic orientations, void shape and material behavior at grain boundaries. In order to bridge this modeling gap, two yield criteria for intergranular ductile void growth are proposed. The first one is a GTN-like model derived from limit-analysis which, once calibrated, accounts for spherical voids at the interface of rate-independent crystals. The second one is developed from a variational approach and predicts yielding in viscoplastic crystals containing intergranular ellipsoidal cavities. Both models are validated against a wide database of numerical limit-analysis of porous bi-crystals using a FFT solver. Satisfying agreements are obtained, paving the way to microstructure-informed intergranular ductile fracture simulation. The interplay between plastic yielding inside grains and along grain boundaries is finally studied based on the proposed yield criterion.

*Keywords:* Ductile fracture, Intergranular fracture, Porous grain boundary, Homogenization, Crystal plasticity, Fast-Fourier transform

## 1. Introduction

Void nucleation, growth and coalescence is among the dominant ductile failure modes in metallic alloys and can be transgranular as well as intergranular. In the latter, the phenomenon of void growth and coalescence happens at grain boundaries due to intense intergranular plastic flow (Hornbogen and Kreye, 1982; Vasudévan and Doherty, 1987). In that case, fracture surfaces display intergranular facets covered in fine dimples. Reliable physical observations of ductile intergranular fracture date back more than fifty years (Plateau et al., 1957) and span a large class of metallic alloys and loading conditions. However, due to insufficient magnification, these facets may appear flat at first glance and can be mistakenly identified as proof of intergranular brittle fracture, impairing comprehensive identification of intergranular ductile fracture occurrences (Lynch, 1991).

Precipitation-hardened alloys are specially prone to dimpled intergranular fracture at low homologous temperature, regardless of crystal lattice structures (Table 1). First and foremost, aluminum alloys are the class of material for which this fracture mode was first undoubtedly highlighted (Varley et al., 1957; Thomas and Nutting, 1957, 1959; Unwin and Smith, 1969). Among the most cited alloys: Al-Zn-Mg (Vasudévan and Doherty, 1987), Al-Zn-Mg-Cu (Kuramoto et al., 1996) and Al-Mg-Si (Poole et al., 2019; Ringdalen et al., 2021). Aluminum alloys containing lithium, divided in three successive generations, form a whole class of materials vulnerable to intergranular fracture by growth and coalescence of cavities (Suresh et al., 1987; Vasudévan and Doherty, 1987; Lynch et al., 2002; Pasang et al., 2012; Decreus et al., 2013). All precipitation-hardened aluminum alloys display precipitate-free zones (PFZ) around grain boundaries; softer than grain interiors, they play an important role in the localization of plasticity (Gräf and Hornbogen, 1977; Vasudévan and Doherty, 1987). The second most common occurrence of intergranular ductile fracture is in nickel superalloys: for instance, Inconel X-750 (Mills, 1980), MAR-M200 (Vasudévan and Doherty, 1987) and Inconel 718 (Chang et al., 2014; Lin et al., 2017). The absence of PFZ in some of these alloys uncovers another elementary phenomenon in which grain boundary precipitation is so detrimental that intergranular soft zones are not needed to foster grain boundary cavity growth (Vasudévan and Doherty, 1987). Similar behaviors are observed in other metallic materials: magnesium alloyed with rare earth elements (*e.g.* Mg-11Gd-2Nd-0.4Zr) experiences this failure mode at specific precipitation aging (Zheng et al., 2008); metastable $\beta$-titanium alloys exhibit dimpled intergranular fracture due to grain boundary precipitates of phase $\alpha$, which is a hurdle to their wider use in aerospace field (Foltz et al., 2011).

Leaving precipitation aging aside, overheating of sulfur-rich steels during austenitization favors intergranular ductile fracture by enhancing grain boundary MnS precipitation (Tsun, 1953; Schulz and McMahon, 1973). Besides, intergranular ductile fracture may be promoted by neutron irradiation (Hojná, 2017), especially when helium bubbles form at grain boundaries, as reported in austenitic steels (Miura et al., 2015) and Nickel-based alloys (Judge et al., 2012, 2015; Demkowicz, 2020). Finally, for the sake of completeness, it should be noted that intergranular fracture at high homologous temperature can also be classified as ductile fracture when purely plastic contributions exceed the intensity of diffusion phenomena associated with creep (Pavinich and Raj, 1977; Riedel, 1987; Kassner and Hayes, 2003). Examples of such

*Corresponding author: cedric.senac@polytechnique.org

situations may be the high strain rate deformation (Fu and Zhang, 2020) and stress-relief cracking (Hornbogen and Kreye, 1982; Chabaud-Reytier et al., 2003) of austenitic steels and the fracture of Inconel X-750 (Venkiteswaran and Taplin, 1974; Mills, 1980).

Table 1: Typical literature observations of low homologous temperature dimpled intergranular fracture in precipitation-hardened alloys for different crystal structures: face-centered cubic (FCC), body-centered cubic (BCC) and hexagonal close-packed (HCP). $f_p$ is the volume fraction of grain boundary precipitates in an inter-crystalline layer of half-width equal to the mean distance between grain boundary precipitates.

| Crystal lattice | **FCC:** peak-aged Al-4.5Mn-1.5Cu (Kuramoto et al., 1996) | **BCC**: lamellar Ti-5Al-5Mo-5V-3Cr-0.5Fe (Foltz et al., 2011) | **HCP:** aged Mg-11Gd-2Nd-0.4Zr (Zheng et al., 2008) |
|---|---|---|---|
| Grain boundary | 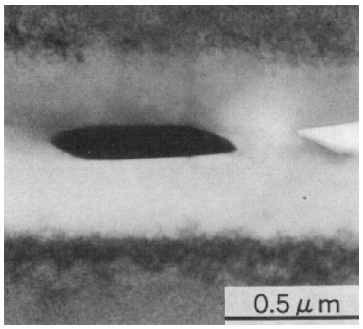 | 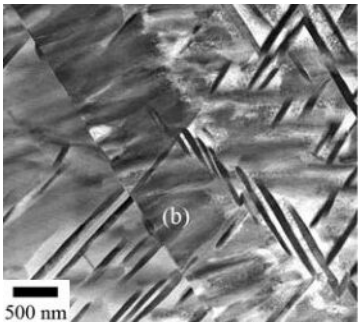 | 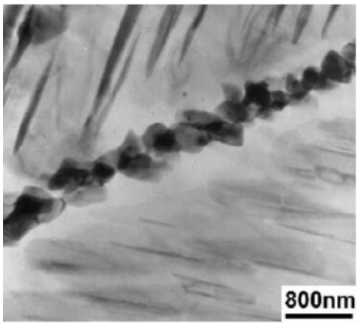 |
| Fracture surface | 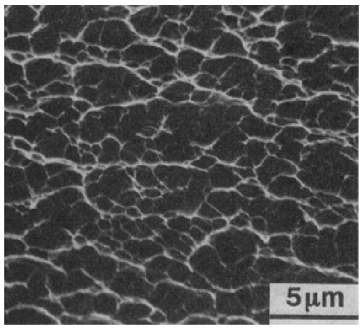 | 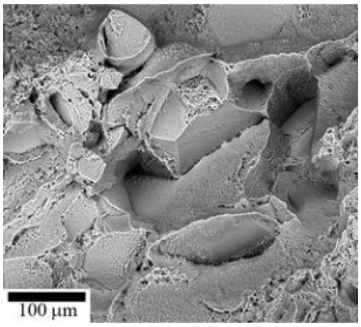 | 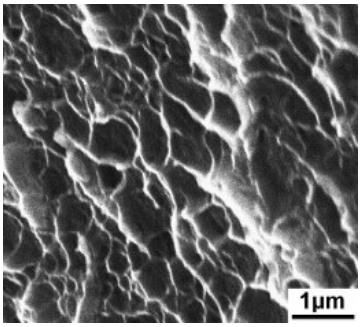 |
| $f_p$ | 0.05 | 0.1 | 0.5 |

Since the seminal works of Rice and Tracey (1969), Gurson (1977) and Thomason (1985), considerable efforts have been made to model ductile failure through homogenization of the mechanical behavior of porous materials, and extensive reviews were published on the matter (Besson, 2010; Benzerga and Leblond, 2010; Pineau et al., 2016). Results contained therein, which mainly concern voids in isotropic or Hill materials, have been extended to single crystals with internal cavities in the last decade (Han et al., 2013; Paux et al., 2015; Mbiakop et al., 2015a; Ling et al., 2016; Song and Ponte-Castañeda, 2017a; Hure, 2019; Khavasad and Keralavarma, 2021). All these studies consider homogeneous matrix materials and are thus designed to model transgranular fracture. Nevertheless, GTN model, relevant for isotropic porous materials, was used to conduct finite element computations of intergranular ductile fracture in precipitation-hardened alloys, either with void-nucleating boundaries and pristine grains (Becker et al., 1989; Molkeri et al., 2020), or with different material parameters in the PFZ and in the grain interior (Pardoen et al., 2003, 2010; Fourmeau et al., 2015) to study competition between fracture modes. Use of this yield function was also made in the context of metastable $\beta$-titanium alloys (Osovski et al., 2015; Li et al., 2017). These models rely on volume homogenization, but grain boundaries are two-dimensional domains; Becker et al. (1989) recommend setting the width of the homogenized microstructure to grain boundary precipitate spacing: conventional precipitate volume fraction $f_p$ is reported in Table 1 for alloys taken as examples. The outcomes of these first studies are valuable but show some limitation. First, numerical homogenization have shown that macroscopic yield surfaces of macroscopically isotropic polycristalline aggregates with intergranular voids are quite distinct from the ones obtained by supposing that voids are in a von Mises isotropic matrix (Lebensohn et al., 2011; Nervi and Idiart, 2015). Then, at the mesoscale of the porous boundaries, all isotropic models previously mentioned are intrinsically not adapted to model complex effects coupling crystallographic orientations, material non-linearity and void size/shape. The isotropic ductile modeling approach is therefore challenged for both macroscopic and mesoscopic applications.

From the earliest times of porous materials homogenization, unit-cell computations have accompanied analytic developments by providing numerical evaluations of yield surfaces (Koplik and Needleman, 1988), which is of paramount importance for the calibration and validation of models. Following their successful application to isotropic and monocrystalline matrices, finite strain unit-cell simulations were only performed on voided bi-crystals in a handful of studies. The majority of these works focused on the void growth stage, *i.e.* deformation situations where plasticity is diffuse and cavities do not not significantly interact with each other in the periodic void lattice; face-centered cubic (FCC) crystals were mostly considered (Wen and Yue, 2007; Zhang et al., 2008; Liu et al., 2009; Li et al., 2015; Dakshinamurthy et al., 2021) except for one study which conducted simulations on a body-centered cubic (BCC) material (Jeong et al., 2018). Void coalescence — *i.e.* the stage in which plasticity localizes in ligaments between cavities — was considered in FCC bi-crystals in Liu et al. (2010). The main conclusion to be drawn is the fact that void growth at grain boundaries is not reducible to void growth in single crystals, all the more to void growth in an isotropic matrix.

Both unit-cell computations and homogenized modeling of ductile intergranular fracture have focused on (initially) spherical voids. However, void shape is known to play an important role when voids significantly differ from ideal spheres (Mbiakop et al., 2015a; Song and Ponte-Castañeda, 2017b), *i.e.* approximately when one of the void axes ratios exceed 2. For smaller deviations from sphericity, the effect on yield surfaces is deemed negligible and yield criteria developed for spherical cavities keep their validity (Hure, 2021). Experimental observations of intergranular void shapes during grain boundary ductile fracture is tricky and, to the knowing of the authors, has never been conducted. Dimples seen on fracture surfaces are usually quite round (see Table 1), which may advocate for spheroidal cavities of symmetry axis perpendicular to the grain boundary. The fact that precipitates responsible for intergranular void nucleation are usually elongated along grain boundaries (Vasudévan and Doherty, 1987; Kuramoto et al., 1996) also suggest such void shapes. On the other hand, helium bubbles involved in the intergranular ductile fracture of irradiated metals are spherical (Miura et al., 2015).

It is therefore concluded that in order to enhance understanding and simulation of intergranular ductile fracture, there is a need for models predicting the yield surface of porous grain boundaries, with both spherical and ellipsoidal cavities; this is the goal set to the present study.

The paper is organized as follows: in a first part, a database of porous bi-crystal unit-cell limit-analysis simulations is gathered and described for a FCC material, including a larger set of crystallographic orientation couples and microstructure parameters than currently available in the literature. In a second part, a Gurson-type yield criterion for the growth of intergranular spherical voids is derived through limit-analysis, along with heuristic corrections of the hydrostatic and the deviatoric terms. In the last part, a gauge surface accounting for intergranular ellipsoidal void shapes is obtained using a variational method. The results of the two yield functions are assessed against numerical homogenization results obtained in the first part. Finally, the implications of those models regarding the competition between intergranular and transgranular failure are briefly discussed.

## 2. Numerical homogenization

In the following, vectors are shown as $\underline{a}$ of norm $a$, second-order tensors as $\boldsymbol{a}$ and fourth-order tensors as $\mathbb{A}$, although $\mathbb{R}$ and $\mathbb{Z}$ still respectively refer to the set of real numbers and the set of integers — they shall be superscripted with a star if 0 is excluded from the set. Numerical limit-analysis simulations are performed in order to assess yield surfaces of porous grain boundaries (Madou and Leblond, 2012); small strain assumption is thus used. Such kind of simulations differ from those existing in the porous bi-crystal literature (*e.g.* Dakshinamurthy et al. (2021)) as the idea is to evaluate yield stress for fixed parameters, either geometrical or material-based (perfect plasticity). Crystal plasticity constitutive laws modeling the grains are first described, then the unit-cells considered are detailed. $\boldsymbol{\sigma}$ stands as the (Cauchy) stress tensor.

### 2.1. Crystal plasticity constitutive laws

Additive decomposition of the total strain into elastic and plastic parts $\boldsymbol{\varepsilon} = \boldsymbol{\varepsilon}^{\mathrm{el}} + \boldsymbol{\varepsilon}^{\mathrm{p}}$ is considered, and elasticity obeys an isotropic Hooke law of Young modulus $Y = 10^3$ MPa and Poisson ratio $\nu = 0.49$. Plasticity is assumed to be related to the glide of dislocations, that can happen in a limited number of directions, called crystallographic slip systems, defined by a slip plane (whose normal is along unit vector $\underline{m}_s$) and a slip direction (of unit vector $\underline{n}_s$), and represented by the following symmetric Schmid tensor : $\boldsymbol{\mu}_s = \frac{1}{2}(\underline{m}_s \otimes \underline{n}_s + \underline{n}_s \otimes \underline{m}_s)$. Other plasticity mechanisms such as twinning are disregarded. A face-centered cubic (FCC) material is considered for numerical homogenization, with $K = 12$ independent slips systems — the $\{111\}\langle 110\rangle$ family. Using viscoplastic regularization, the plastic strain rate writes (Hutchinson, 1976):

$$\dot{\boldsymbol{\varepsilon}}^{\mathrm{p}} = \sum_{s=1}^{K} \left[ \dot{\gamma}_0 \left( \frac{\left| \boldsymbol{\sigma} : \boldsymbol{\mu}_s \right|}{\tau_s^{\mathrm{c}}} \right)^n \mathrm{sgn}(\boldsymbol{\sigma} : \boldsymbol{\mu}_s) \right] \boldsymbol{\mu}_s = \sum_{s=1}^{K} \dot{\gamma}_s \boldsymbol{\mu}_s \tag{1}$$

where $\tau_s^{\mathrm{c}}$ is the critical resolved shear stress of the $s^{\mathrm{th}}$ system, $\dot{\gamma}_0$ a reference slip-rate (set to $1\ \mathrm{s}^{-1}$) and $\dot{\gamma}_s$ the slip rate of system $s$. $(\tau_s^{\mathrm{c}})$ are fixed to the same value of $\tau^{\mathrm{c}} = 88$ MPa. $n$ denotes the Norton exponent: the case $n \to +\infty$ corresponds to rate-independent plasticity while $n = 1$ represents linear Maxwell-type viscoelasticity. In the following, the value $n = 100$ will be chosen to stand for rate-independence.

### 2.2. Unit-cell computations

In order to study the mechanical behavior of porous grain boundaries, different periodic unit-cells can be chosen. Note that grain boundaries are not perfectly periodic structures, but this assumption is required by the FFT solver used. A microstructure composed of two single crystals of different crystallographic orientations (phases 1 and 2) regularly laminated along direction $\underline{e}_1$ and with periodic square arrays of cavities (phase 0) at $(\underline{e}_2, \underline{e}_3)$-grain boundaries is considered. Porosity — *i.e.* void volume fraction — is denoted $f$. Perfect bounding is assumed between the crystals. Such a periodic distribution corresponds to the configuration shown in Fig. 1b, the width of crystal layers taken equal to the spatial period of cavities along $\underline{e}_2$ and $\underline{e}_3$. A simple way of alleviating computational burden consists in inserting cavities at every other boundary, leading to the cubical geometry of Fig. 1a and dividing the unit-cell volume by two, provided that the two configurations approximately lead to the same predictions; such an assumption will be discussed in the following. Other configurations shown on Figs. 1c,d,e will be studied later. Single crystals behavior is the one presented in Section 2.1 while cavities are modeled as an elastic material of vanishing stiffness tensor.

Simulations are performed in the fast Fourier transform-based `AMITEX_FFTP` code (CEA, 2022) using periodical boundary conditions. Unit-cells are discretized using cubical voxels. A unique material behavior (void, crystal 1 and

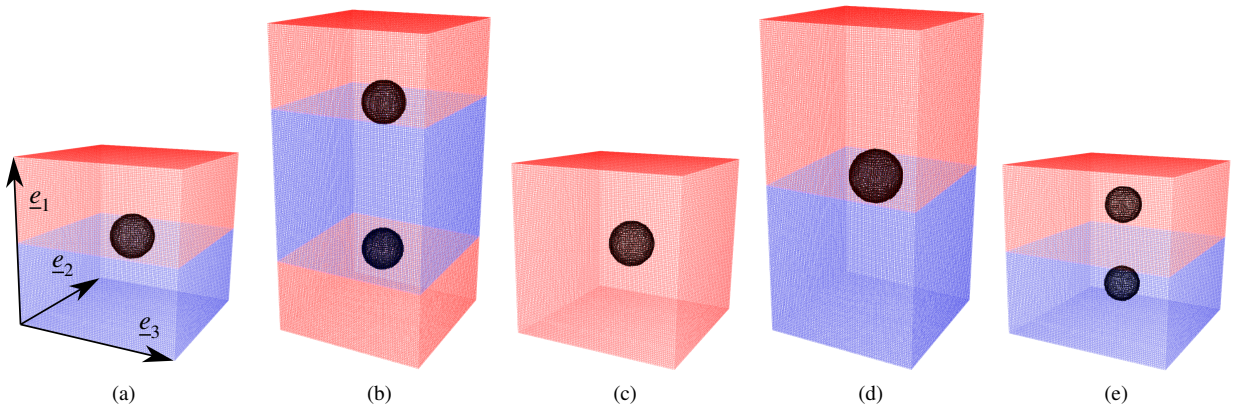


Figure 1: Periodic unit-cell configurations considered in the numerical limit analysis: (a) porous boundary; (b) symmetric porous boundary, (c) porous single crystal, (d) elongated porous boundary and (e) porous laminate. Single crystals are shown in red/blue and cavities in black. All are pictured with 1% porosity and spherical voids.

crystal 2) is assigned to each of the voxels. Application and validation of FFT numerical methods for (porous) crystals can be found in previous studies (Barrioz, 2019; Barrioz et al., 2019). Unit-cells are subjected to the macroscopic (volume-average) stress tensor $\mathbf{\Sigma}$ whose principal axes are aligned with unit-cell lattice directions and whose main stress component[1] is along $\underline{e}_1$:

$$\mathbf{\Sigma} = \Sigma_{11}\mathbf{\Sigma}^{(0)}(T,\theta) = \frac{\Sigma_{11}}{\cos\theta + \frac{3}{2}T}\begin{pmatrix} \cos\theta + \frac{3}{2}T & 0 & 0 \\ 0 & -\cos\left(\theta + \frac{\pi}{3}\right) + \frac{3}{2}T & 0 \\ 0 & 0 & -\cos\left(\theta - \frac{\pi}{3}\right) + \frac{3}{2}T \end{pmatrix} \tag{2}$$

where $T$ is the stress triaxiality — *e.g.* the ratio between hydrostatic stress $\Sigma_{\mathrm{m}}$ and von Mises equivalent stress $\Sigma_{\mathrm{eq}}^{\mathrm{vM}}$ — and $\theta$ is the Lode angle defined as (Danas and Ponte Castañeda, 2012):

$$\cos 3\theta = \frac{27}{2}\frac{\det\left(\mathbf{\Sigma} - \Sigma_{\mathrm{m}}\boldsymbol{I}\right)}{\left(\Sigma_{\mathrm{eq}}^{\mathrm{vM}}\right)^3} \tag{3}$$

with $\theta \in \{0, \pi/3\}$ corresponding to axisymmetric loadings and $\theta = \pi/6$ to in-plane shear loadings. The loading is controlled by the linear increase of (volume-average) strain component $E_{11}$ until small strain yielding of the unit-cell, which manifests by the saturation of $\mathbf{\Sigma}$ to values corresponding to the yield stress of the unit-cell (see Fig. 2a). The macroscopic strain rate component $D_{11}$ is set to 0.05 $\mathrm{s}^{-1}$. In the limit $n = +\infty$, yield surfaces do not depend on this strain rate. Note that the elastic behavior of the crystals have no influence on the plastic yielding —- *i.e.* on the saturated value of $\mathbf{\Sigma}$. In that sense, these unit-cell simulations are consistent with the theoretical framework of limit-analysis (Leblond et al., 2018).

Upon saturation, von Mises equivalent stress $\Sigma_{\mathrm{eq}}^{\mathrm{VM}}$ and mean stress $\Sigma_{\mathrm{m}}$ are computed to draw the yield surface in the $\left(\Sigma_{\mathrm{m}}, \Sigma_{\mathrm{eq}}^{\mathrm{VM}}\right)$ meridian plane. The typical numerical yield surface of a porous material is shown in Fig. 2b. Unit-cell simulations can be divided in two groups according to the deformation mode they display. Low stress triaxiality ratios correspond to diffuse plasticity (see Appendix B, Fig. B.15a) whereas localized plasticity occurs at high triaxiality ratios (see Appendix B, Fig. B.15c). The first deformation mode is referred to as void growth while the second is called void coalescence (Pineau et al., 2016): on Fig. 2b, the relevant mode is indicated for each numerical simulation — from now on, simulations involving coalescence will be identified as hollowed-out symbols. Details on the determination of the deformation mode of a given unit-cell simulation are given in Appendix B. In most studies in the literature, separate yield criteria are proposed to describe them; within a multi-surface plasticity framework, these yield criteria are considered simultaneously (Benzerga and Leblond, 2010; Keralavarma, 2017). Coalescence criteria are usually variations over Thomason's model (Thomason, 1985) which sets a limit value to the main principal macroscopic stress $\Sigma_{\mathrm{I}}$. Thus, these models manifest as straight lines[2] in the meridian place (see Fig 2b). Since the objective of this study is to provide a void growth model, the analytical yield surface will be checked to reproduce simulations displaying growth (full points) but special care will also be taken that the criterion is *exterior* to simulations displaying coalescence (hollowed-out points) in order for the multi-surface plasticity approach to be effective.

### 2.3. Simulation database

As in the case of porous single crystals (Sénac et al., 2022), yield surfaces are expected to significantly depend on crystallographic orientations. Therefore, forty random orientations gathered in twenty couples are studied here; see

[1] In the cases considered below, $\cos\theta + \frac{3}{2}T$ never vanish; such a situation would mean that the loading should be controlled using another principal axis.

[2] Taking the equivalent von Mises stress of Eq. 2 brings $\Sigma_{\mathrm{eq}}^{vM}\left(\cos\theta + \frac{3}{2}\frac{\Sigma_{\mathrm{m}}}{\Sigma_{\mathrm{eq}}^{vM}}\right) = \frac{3}{2}\Sigma_{11}$, which is a straight-line in a meridian plane, *i.e.* at fixed Lode angle $\theta$.

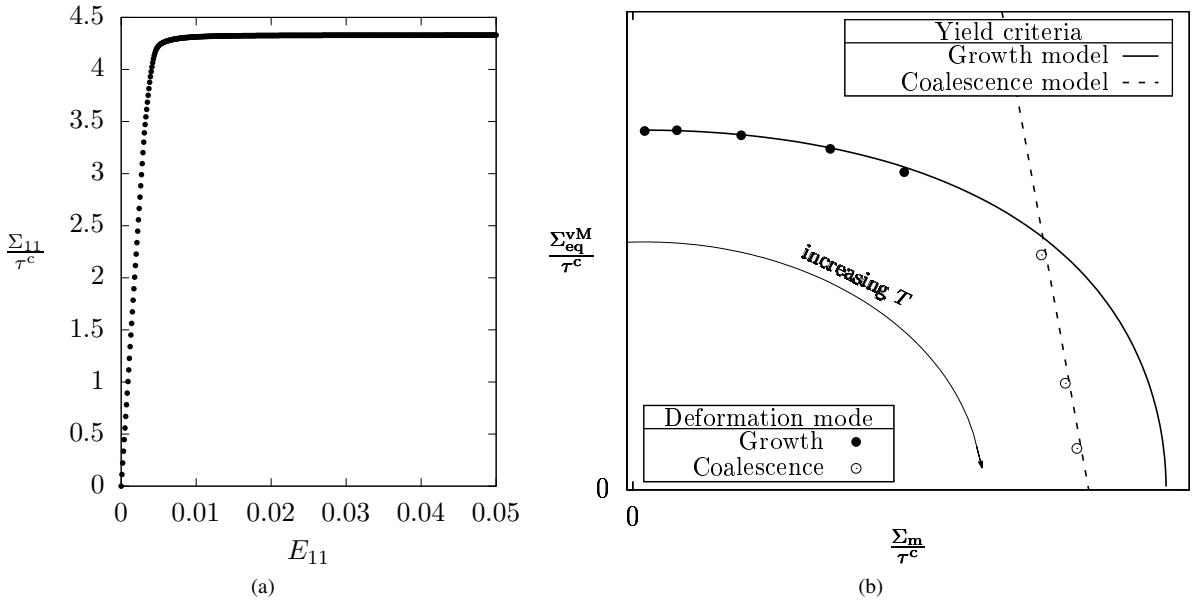


(a) (b)

Figure 2: (a) Stress saturation of $\Sigma_{11}$ occurring during small strain yielding of a porous boundary with orientation couple #1 at $T = 1$, $\theta = 0$ and $f = 0.01$; (b) Sketch of a typical numerical yield surface (points) in a meridian half-plane (fixed $\theta$), along with multi-surface plasticity modeling approach (lines).

Table 2 for their definition and colors with which they will be represented in all subsequent graphs. For fixed Lode angle $\theta$, visualization of yield surfaces will be made in the plane $(\Sigma_m, \Sigma_{eq}^{vM})$, *i.e.* by considering various stress triaxialities. This corresponds to yield surfaces meridian half-planes. Since the matrix material behaves similarly under tension and compression, the macroscopic yield surface is centrally symmetric (*i.e.* the yield stress for $(T, \theta)$ is equal to that at $(-T, \pi/3 - \theta)$) so that it is enough to study the set of loadings for which $T > 0$ and $\theta \in [0, \pi/3]$. To cover the range from deviatoric stress-state to hydrostatic loading, $T$ takes the following values: 0, 1/3, 1, 2, 3, 6, 10, 40.

Table 2: Euler angles (Bunge convention) of the 20 couples of random crystallographic orientations.

| | # | Crystal 1 | | | Crystal 2 | | |
|---|---|---|---|---|---|---|---|
| | | $\phi_1$ (°) | $\Phi$ (°) | $\phi_2$ (°) | $\phi_1$ (°) | $\Phi$ (°) | $\phi_2$ (°) |
| ● | 1 | 93.48 | 53.17 | 315.41 | 40.96 | 84.69 | 136.94 |
| ● | 2 | 65.60 | 112.22 | 83.99 | 166.48 | 40.56 | 139.94 |
| ● | 3 | 109.49 | 111.84 | 171.00 | 124.35 | 34.17 | 267.58 |
| ● | 4 | 117.83 | 107.35 | 66.79 | 141.70 | 100.97 | 29.13 |
| ● | 5 | 16.78 | 55.01 | 63.50 | 142.68 | 53.37 | 29.46 |
| | 6 | 11.08 | 98.29 | 28.20 | 303.92 | 75.55 | 149.39 |
| | 7 | 134.39 | 133.33 | 7.13 | 266.58 | 63.38 | 310.06 |
| | 8 | 306.96 | 149.84 | 66.68 | 243.19 | 117.06 | 258.27 |
| ● | 9 | 229.38 | 96.02 | 323.86 | 102.10 | 81.67 | 264.81 |
| ● | 10 | 145.96 | 121.95 | 3.42 | 103.35 | 82.43 | 137.59 |
| | 11 | 73.67 | 120.61 | 85.47 | 302.65 | 57.31 | 202.39 |
| | 12 | 18.40 | 105.32 | 226.75 | 268.41 | 94.25 | 240.26 |
| ● | 13 | 80.74 | 111.44 | 185.63 | 192.59 | 45.76 | 0.65 |
| | 14 | 352.79 | 112.15 | 125.60 | 228.63 | 93.54 | 261.97 |
| | 15 | 70.28 | 56.03 | 22.94 | 70.74 | 76.48 | 243.32 |
| ● | 16 | 81.82 | 113.92 | 64.02 | 80.34 | 65.46 | 267.16 |
| | 17 | 120.04 | 67.52 | 178.16 | 328.21 | 119.29 | 201.63 |
| | 18 | 129.85 | 49.16 | 99.07 | 296.23 | 120.50 | 328.96 |
| | 19 | 230.74 | 161.52 | 140.50 | 81.97 | 64.24 | 149.44 |
| | 20 | 345.16 | 129.65 | 267.30 | 154.50 | 61.95 | 181.57 |

The equivalence of unit-cell configurations displayed in Fig. 1a,b was checked on representative cases: no noticeable difference was seen on yield surfaces. This finding is no surprise: as long as cavities do not interact with each other between distinct $(\underline{e}_2, \underline{e}_3)$-planes (*e.g.* by necklace coalescence or out-of-plane shear-banding), the upper part of Fig. 1b is independent from the lower part, thus both will have the same behavior as Fig. 1a.

Before studying extensively porous bi-crystals, it is useful to assess differences between a porous grain boundary (Fig. 1a) and porous single crystals (Fig. 1c) of crystallographic orientations corresponding to the two constitutive grains of the bi-crystal. This was performed with spherical cavities considering all orientation couples with Norton exponents $n = 1$, 3, 10 and 100. Only data for $n = 100$ are shown on Fig. 3 as other $n$ displayed similar tendencies. An obvious

remark is that a porous bi-crystal yield surface is reducible to neither of its crystal constituents' individual behaviour, justifying the present study. Such a finding was already reported by Jeong et al. (2018) and Dakshinamurthy et al. (2021) who described porous bi-crystals showing intermediate yield stress compared to the two individual porous grains, corresponding to Fig. 3a. However, due the small number of orientation couples and triaxiality ratios studied in the existing literature, other possible bi-crystal behaviors were overlooked: in Fig. 3b, the yield stress of the porous bi-crystal is greater than yield stresses of both porous single crystals from low to medium stress triaxialities and smaller at high triaxialities. However, in no instance was the porous bi-crystal yield stress smaller than both porous grain yield stresses for deviatoric loadings. This property shall be demonstrated in the limit of small porosities in Appendix C. Overall, for random orientations, spherical voids, axisymmetric loading conditions and triaxialities ranging from $T = 0$ to $T = 3$, plastic yielding seems to occur for lower stress in at least one of the porous single crystal compared to the porous boundary. Such a general rule hints at the fact that a material with homogeneous porosity is more susceptible to transgranular ductile fracture than to intergranular ductile fracture; in order for such a failure mode to arise, boundaries have to be weakened compared to grain interiors: for instance greater porosity, different void shape, softer behavior, lower hardening capacity (see Pardoen et al. (2003) on that subject).

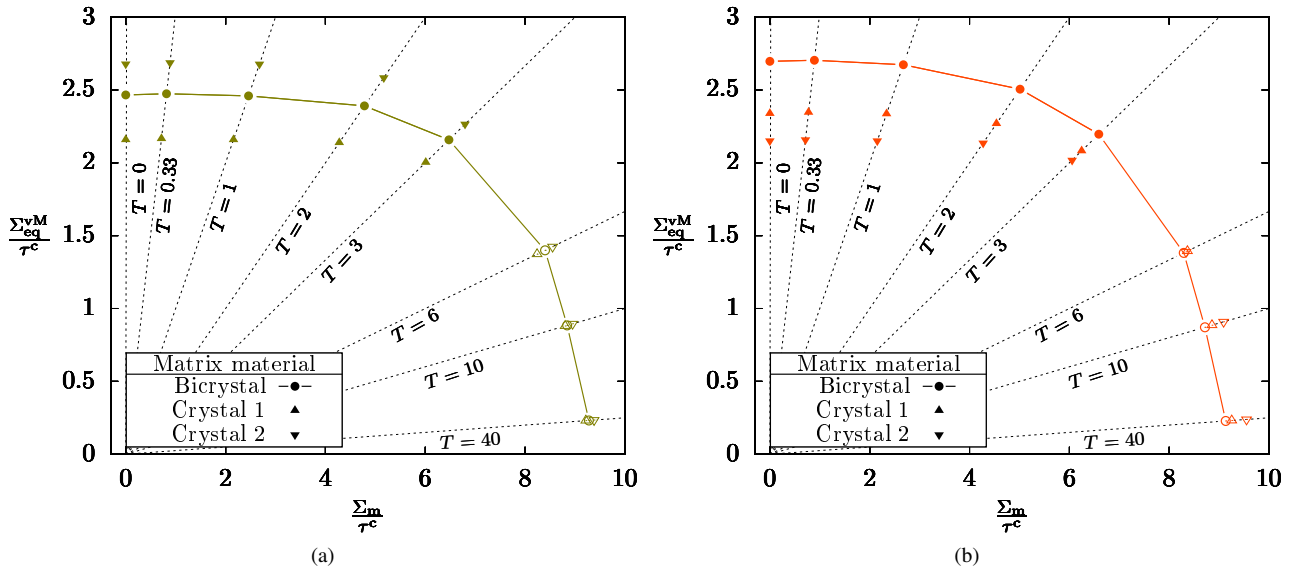


Figure 3: Yield surfaces of porous bi-crystals (Fig. 1a) and corresponding porous constitutive single crystals (Fig. 1c) at $f = 0.005$, $n = 100$ and $\theta = 0$: (a) crystal orientation couple #3; (b) crystal orientation couple #2. Hollowed-out symbols mark simulations in which the deformation mode has been identified as void coalescence.

Since void growth yield criteria for single crystals are available, a legitimate question is whether such models could account for porous boundaries by delocalizing the cavity from either side of the interface. Instead of a unique void of volume $f$ – the unit-cell has a volume of 1 – set at mid-height, voids of volume $f/2$ are located at mid-width of each crystal, effectively turning Fig. 1a into Fig. 1e. As shown in Fig. 4a, the porous laminate unit-cell (Fig. 1e) yield surface diverges significantly at high triaxialities from the porous boundary (Fig. 1a) yield surface. The wider stress reversibility domain of the former makes it impossible to invoke earlier coalescence to explain such a discrepancy: unit-cells *do* have a different void growth behavior, with voids located at grain boundaries being more damaging than voids inside grains[3]. For lower Norton exponents $n$ (Eq. 1), discrepancies are smaller but still noticeable.

Finally, a necessary verification is to quantify the effect of unit-cell aspect ratio at fixed porosity: if this effect is negligible, simulations can be restricted to cubic cells. This is done by comparing Fig. 1b,d unit-cell yield surfaces in Fig. 4b. No noticeable discrepancy is seen from low to intermediate triaxialities between the two configurations. However, as the cavities are closer in the plane $(\underline{e}_2, \underline{e}_3)$ in the configuration Fig. 1d, coalescence is more intense, leading to a strong contraction of the yield surface near the hydrostatic point. Since this deformation mode is not the subject of this study, it shall be considered in the following that unit-cell height — and more generally unit-cell geometry, see the discussion in Danas and Castañeda (2009) — has no effect on void growth plastic yielding.

Given the preliminary results gathered in this section, Fig. 1a unit-cell configuration is chosen to assess void growth yield surfaces of porous grain boundaries. Using this unit-cell, three batches of simulations were conducted with the aforementioned set of crystal orientations and triaxiality ratios: a first set of computations was carried out with spherical voids at porosities $f \in \{0.001, 0.005, 0.01, 0.05, 0.1, 0.2, 0.3\}$ and $\theta = 0$; a second considered spherical voids at fixed porosity $f = 0.01$ but with a larger set of loadings: on the one hand $\theta \in \{\pi/6, \pi/3\}$ and on the other hand $\theta = 0$ with $\boldsymbol{\Sigma}$ subjected to rotations around $\underline{e}_2$ of $\alpha = \pi/4$ (main stress axis along $\underline{e}_1 + \underline{e}_3$) and $\pi/2$ (main stress axis along $\underline{e}_3$). Finally, simulations of ellipsoidal cavities were conducted at $\theta = 0$ and $f = 0.01$; more details on these geometries will be given in Section 4. The ensuing database holds 800 simulations to validate the models. The results of the simulations will be presented when compared to theoretical results in the next sections.

[3]Note that is not in contradiction to what have been said earlier about porous single crystals: voids in Fig. 1e crystals are smaller so that both unit-cells Fig. 1a,e have equal void volume fractions.

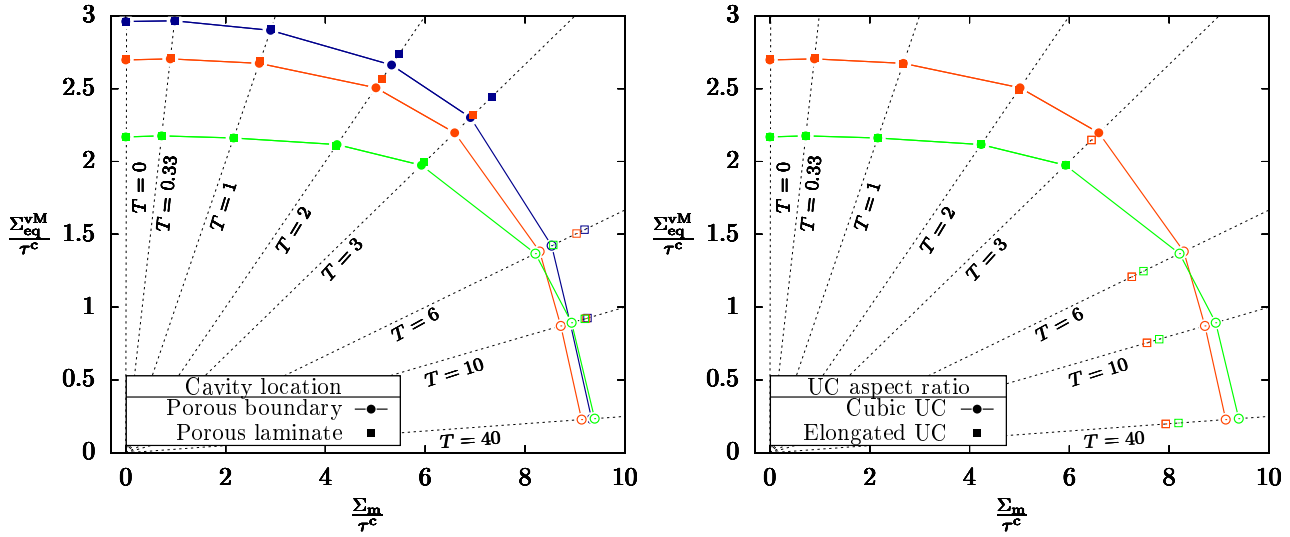


Figure 4: Yield surfaces for different unit-cell configurations at $f = 0.005$, $n = 100$ and $\theta = 0$: (a) effect of void location (Fig. 1a versus Fig. 1e); (b) effect of unit-cell aspect ratio (Fig. 1a versus Fig. 1d). Hollowed-out symbols mark simulations in which the deformation mode has been identified as void coalescence.

Since spherical cavities are discretized into cubic voxels, mesh convergence has to be checked. Cube edge discretization of $N = 300$ at $f = 0.01$ (which corresponds approximately to a cavity radius $r$ of 30 voxel length) is taken as the converged value. Comparisons with $N = 45$ (6 voxels), 85 (10 voxels) and 150 (20 voxels) uncover respective maximum relative errors of 1.9%, 1.1%, and 0.5%. Given these findings, values $N = 85$ ($f \geq 0.01$), 95 ($f = 0.005$) and 162 ($f = 0.001$) are chosen for unit-cell containing spherical cavities[4]; similar considerations about minimum semi-axis drive the choice of mesh discretization for ellipsoidal cavities.

A first model is developed in the next section to predict yield surfaces of porous bi-crystals with spherical voids in the rate-independent limit.

## 3. Plastic yield criterion for spherical voids

In this section, an approximate yield criterion is proposed for rate-independent ($n \to +\infty$) porous bi-crystals with spherical voids using limit analysis. The yield function of a perfect crystal is regularized according to Arminjon (1991) and Gambin (1991):

$$\mathcal{F}_m^{\text{mono}}(\boldsymbol{\sigma}) = \left[\sum_{s=1}^{K}\left(\frac{|\boldsymbol{\sigma}:\boldsymbol{\mu}_s|}{\tau_s^c}\right)^m\right]^{2/m} - 1 \tag{4}$$

In the limit $m \to +\infty$, Schmid law is recovered. As stated in Paux et al. (2015), taking $m = 2$ in Eq. 4 amounts to approximating the perfect crystal with a Hill-type material (Hill, 1948). This reduction is likely to be crude, but adopting it will allow to derive a yield criterion in Section 3.1. Then, following a suitable heuristic, this yield surface will be adapted to the case $m \to +\infty$ in Section 3.2.

In the analyses conducted in this section and the following one, the hypothesis that ($\tau_s^c$) are close to their mean $\tau^c$ is made; this will allow substitution of $\tau_s^c$ by $\tau^c$ and *vice-versa* whenever it is necessary in the calculations. This assumption seems acceptable in FCC materials but may be an issue in some HCP materials (Song and Ponte-Castañeda, 2017b).

### 3.1. Limit-analysis on porous Hill bi-materials

Following the limit-analysis framework used by Gurson (1977) for porous isotropic materials and specialized to porous Hill materials by Benzerga and Besson (2001), we consider a representative volume element of a material containing three phases $i$ occupying volumes $\Omega_i$, as pictured in Fig 5. Phase 0 is a cavity of vanishing stiffness and volume fraction $f = (a/b)^3$ and phases 1 and 2 are perfectly plastic Hill materials of yield functions:

$$\mathcal{F}_2^{(i)}(\boldsymbol{\sigma}) = \left(\sigma_{\text{eq}}^{\text{H}}\right)^2 - 1 = \frac{3}{2}\boldsymbol{\sigma}:\mathbb{H}_i:\boldsymbol{\sigma} - 1 \tag{5}$$

where $\mathbb{H}_i$ are Hill stress anisotropy tensors — notice that contrary to the common formulation, they are *not* dimensionless. Matrix materials are incompressible, thus $\mathbb{J}:\mathbb{H}_i = \mathbb{H}_i:\mathbb{J} = 0$ with $\mathbb{J} = \frac{1}{3}\boldsymbol{I}\otimes\boldsymbol{I}$. For each material $i$, the associated equivalent strain rate is $d_{\text{eq}} = \sqrt{\frac{2}{3}\boldsymbol{d}:\mathbb{H}_i^*:\boldsymbol{d}}$ with $\mathbb{H}^*$ a tensor verifying $\mathbb{H}^*:\mathbb{H} = \mathbb{H}:\mathbb{H}^* = \mathbb{K}$, where $\mathbb{K} = \mathbb{I} - \mathbb{J}$. In a base of orthotropy, the components of $\mathbb{H}^*$ can be obtained from the components of $\mathbb{H}_i$ following the formulas given in Morin (2012) (Appendix A.2). More fundamentally, $\mathbb{H}^*$ is linked to $\mathbb{H}$ through linear algebra, as shown in Appendix A of the present work.

[4] To be compared with 3, 16 and 32 voxels per cavity radius used respectively in Hure (2021), Vincent et al. (2014) and Wojtacki et al. (2020).

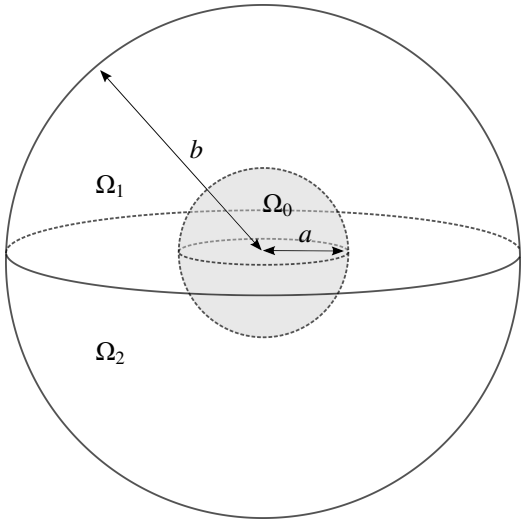


Figure 5: Spherical unit-cell with spherical cavity, used for the limit-analysis.

The unit-cell being subjected to prescribed uniform strain rate $\boldsymbol{D}$ on its boundary, the set $\mathcal{K}(\boldsymbol{D})$ of incompressible microscopic strain rate fields which are kinematically admissible with $\boldsymbol{D}$ is considered. The microscopic plastic dissipation associated to such a strain rate field $\dot{\boldsymbol{\varepsilon}}$ is :

$$\begin{aligned} \varpi\left(\dot{\boldsymbol{\varepsilon}}\left(\underline{x}\right)\right) &\equiv \sup_{\widehat{\boldsymbol{\sigma}}\in\mathcal{C}\left(\underline{x}\right)} \left(\widehat{\boldsymbol{\sigma}} : \dot{\boldsymbol{\varepsilon}}\left(\underline{x}\right)\right) \\ &= \sqrt{\frac{2}{3}\dot{\boldsymbol{\varepsilon}}\left(\underline{x}\right) : \mathbb{H}^*\left(\underline{x}\right) : \dot{\boldsymbol{\varepsilon}}\left(\underline{x}\right)} \end{aligned} \tag{6}$$

where $C\left(\underline{x}\right)$ is the microscopic elasticity domain at point $\underline{x}$.

In the framework of limit analysis, any trial field $\dot{\boldsymbol{\varepsilon}} \in \mathcal{K}(\boldsymbol{D})$ gives an upper bound for the effective dissipation $\Pi$, defined as:

$$\Pi(\boldsymbol{D}) = \inf_{\dot{\boldsymbol{\varepsilon}}\in\mathcal{K}(\boldsymbol{D})} \left\langle \varpi\left(\dot{\boldsymbol{\varepsilon}}\left(\underline{x}\right)\right)\right\rangle_{\cup_i \Omega_i} = \frac{1-f}{2} \inf_{\dot{\boldsymbol{\varepsilon}}\in\mathcal{K}(\boldsymbol{D})} \left[\sum_{i=1}^{2} \left\langle \varpi\left(\dot{\boldsymbol{\varepsilon}}\left(\underline{x}\right)\right)\right\rangle_{\Omega_i}\right] \tag{7}$$

where $< \cdot >$ denotes volume averaging. From that upper bound $\Pi^+$, an approximate yield criterion is obtained since for a given strain rate $\boldsymbol{D}_0$, the macroscopic yield stress $\boldsymbol{\Sigma}$ is defined as the tangent vector to surface $\Pi^+(\boldsymbol{D})$ at point $\boldsymbol{D}_0$ (Suquet, 1982). Walking the footsteps of Benzerga and Besson (2001), the following strain rate field — which was already employed in Gurson (1977) — is chosen and expressed in spherical coordinates $(r, \theta, \phi)$:

$$\dot{\boldsymbol{\varepsilon}} = \dot{\boldsymbol{\varepsilon}}_A + \dot{\boldsymbol{\varepsilon}}_B \quad \text{with} \quad \begin{cases} \dot{\boldsymbol{\varepsilon}}_A\left(\underline{x}\right) &= \dfrac{\mathrm{Tr}(\boldsymbol{D})}{3}\left(\dfrac{b}{r}\right)^3 \left[-2\underline{e}_r \otimes \underline{e}_r + \underline{e}_\theta \otimes \underline{e}_\theta + \underline{e}_\phi \otimes \underline{e}_\phi\right] \\ \dot{\boldsymbol{\varepsilon}}_B &= \mathbb{K} : \boldsymbol{D} \end{cases} \tag{8}$$

Approximation of Eq. 6 used in Benzerga and Besson (2001) relies on the computation of the mean square microscopic plastic dissipation over a sphere $\mathcal{S}(r)$ of radius $r$:

$$\left\langle \varpi\left(\dot{\boldsymbol{\varepsilon}}\right)^2\right\rangle_{\mathcal{S}(r)} = \frac{1}{3}\sum_{i=1}^{2}\left[\dot{\boldsymbol{\varepsilon}}_B : \mathbb{H}_i^* : \dot{\boldsymbol{\varepsilon}}_B + 2\left\langle \dot{\boldsymbol{\varepsilon}}_A\right\rangle_{\mathcal{S}(r)\cap\Omega_i} : \mathbb{H}_i^* : \dot{\boldsymbol{\varepsilon}}_B + \left\langle \dot{\boldsymbol{\varepsilon}}_A : \mathbb{H}_i^* : \dot{\boldsymbol{\varepsilon}}_A\right\rangle_{\mathcal{S}(r)\cap\Omega_i}\right] \tag{9}$$

It is useful to remark that for a point $\underline{x}^1$ located on demi-sphere $\mathcal{S}(r) \cap \Omega_1$ and its symmetrical with respect to the origin $\underline{x}^2$ located on complementary demi-sphere $\mathcal{S}(r) \cap \Omega_2$, the local spherical frames are related: $(\underline{e}_r^2, \underline{e}_\theta^2, \underline{e}_\phi^2) = (-\underline{e}_r^1, \underline{e}_\theta^1, -\underline{e}_\phi^1)$. Given the specific form of $\dot{\boldsymbol{\varepsilon}}_A$, the following relations are obtained:

$$\left\langle \dot{\boldsymbol{\varepsilon}}_A\right\rangle_{\mathcal{S}(r)\cap\Omega_1} = \left\langle \dot{\boldsymbol{\varepsilon}}_A\right\rangle_{\mathcal{S}(r)\cap\Omega_2} = \left\langle \dot{\boldsymbol{\varepsilon}}_A\right\rangle_{\mathcal{S}(r)} \tag{10}$$

Furthermore, it can be verified that:

$$\forall i \in \{1,2\},\ \left\langle \dot{\boldsymbol{\varepsilon}}_A : \mathbb{H}_i^* : \dot{\boldsymbol{\varepsilon}}_A\right\rangle_{\mathcal{S}(r)\cap\Omega_i} = \left\langle \dot{\boldsymbol{\varepsilon}}_A : \mathbb{H}_i^* : \dot{\boldsymbol{\varepsilon}}_A\right\rangle_{\mathcal{S}(r)} \tag{11}$$

Substitution of the present expressions into the development of Benzerga and Besson (2001) leads to the following yield criterion:

$$\left(\frac{3}{2}\boldsymbol{\Sigma} : \left[\frac{1}{2}\mathbb{H}_1^* + \frac{1}{2}\mathbb{H}_2^*\right]^* : \boldsymbol{\Sigma}\right) + 2qf\cosh\left(\frac{3\sqrt{2}}{\sqrt{\chi\left(\mathbb{H}_1^*\right) + \chi\left(\mathbb{H}_2^*\right)}}\Sigma_m\right) - 1 - (qf)^2 = 0 \tag{12}$$

$$\chi(\mathbb{H}^*) = \frac{8}{15}\left(h_{11}^* + h_{22}^* + h_{33}^* - h_{23}^* - h_{31}^* - h_{12}^*\right) + \frac{4}{5}\left(h_{44}^* + h_{55}^* + h_{66}^*\right) \tag{13}$$

where $q$ is Tvergaard's adjustment parameter (Tvergaard, 1982) and $h^*_{ij}$ are components of tensor $\mathbb{H}^*$ in the Voigt-Mandel notation, regardless the chosen geometric frame. Eq. 13 is obtained from the lengthy yet straightforward calculation of $\left\langle \dot{\boldsymbol{\varepsilon}}_A : \mathbb{H}^*_i : \dot{\boldsymbol{\varepsilon}}_A \right\rangle_{S(r)}$ which involves the recasting of $\mathbb{H}^*_i$ from the bi-crystal frame of reference to the local spherical frame of reference. Note that Eq. 13 is not directly found in Benzerga and Besson (2001) since this reference expressed $\chi$ as a function of eigenvalues of $\mathbb{H}$ whereas, in the present work, $\chi$ is a function of coefficients of $\mathbb{H}$ in an arbitrary basis. Equivalence of the two expressions can be obtained using Eq. A.3 presented in Appendix A. Therefore, in the limit where phase 1 and phase 2 are identical, $\left(\mathbb{H}^*_1\right)^* = \mathbb{H}_1$ and the criterion of Benzerga and Besson (2001) for porous Hill materials is recovered.

### 3.2. Porous bi-crystal correction

In the context of Eq. 4 with the approximation $m = 2$, the results of Section 3.1 can be specialized to perfectly-plastic crystals by setting the following stress anisotropy tensors:

$$\mathbb{H}_i = \frac{2}{3}\mathbb{S}_i \quad \text{with} \quad \mathbb{S}_i = \sum_{s=1}^{K} \frac{1}{\left(\tau_s^{(i),\mathrm{c}}\right)^2} \left[\boldsymbol{\mu}_k^{(i)} \otimes \boldsymbol{\mu}_k^{(i)}\right] \tag{14}$$

As stated in Paux et al. (2015), in the case of cubic crystal lattices with equivalent critical resolved shear stresses ($\tau_s^{\mathrm{c}} = \tau^{\mathrm{c}}$), $\mathbb{S}$ is a linear combination of deviatoric cubic projectors[5] $\mathbb{K}'$ and $\mathbb{K}''$ defined in Walpole (1981) with coefficients $(\alpha', \alpha'')$:

$$\mathbb{K}' = \mathbb{G} - \mathbb{J}\,, \quad \mathbb{K}'' = \mathbb{I} - \mathbb{G} \quad \text{where} \quad \mathbb{G} = (\delta_{ij}\delta_{jk}\delta_{kl})_{ijkl} \tag{15}$$

written in the frame of orthotropy. Then, $\mathbb{S}^*$ can be obtained simply as its decomposition coefficients are $(1/\alpha', 1/\alpha'')$. However, crystal 1 and 2 orthotropy axes are not the same so the deviatoric term of Eq. 12 cannot be expressed simply according to cubic projectors. Still, for a FCC crystal with $\tau_s^{\mathrm{c}} = \tau^{\mathrm{c}}$, $(\tau^{\mathrm{c}})^2\alpha' = 2$ and $(\tau^{\mathrm{c}})^2\alpha'' = 2/3$ so that Eq. 13 writes $\chi = 33\,(\tau^{\mathrm{c}})^2\,/5$.

As expected, Eq. 12 is in poor agreement with porous bi-crystal unit-cell computations conducted in Section 2.3 for quasi-rate independent behavior ($n = 100$). Following Paux et al. (2015), independent corrections of hydrostatic and deviatoric terms are conducted.

*Hydrostatic point:* In the case of a FCC single crystal hollow sphere, Paux et al. (2018) determined that the value $\kappa' \equiv 3\tau^{\mathrm{c}}/\sqrt{\chi} \approx 0.49$ was needed to recover the plastic dissipation associated with microscopic strain rate $\dot{\boldsymbol{\varepsilon}} = \dot{\boldsymbol{\varepsilon}}_B$. A similar result ($\kappa' \approx 0.489$) was obtained in Hure (2019) using a simplified derivation. Eq. 16 of the latter reference, specialized to a voided bi-crystal, leads to:

$$\kappa' = \frac{3}{\left\langle M_1\left(\underline{x}, \dot{\boldsymbol{\varepsilon}}_B\right)\right\rangle_{\Omega_1} + \left\langle M_2\left(\underline{x}, \dot{\boldsymbol{\varepsilon}}_B\right)\right\rangle_{\Omega_2}} \quad \text{with} \quad M_i\left(\underline{x}, \dot{\boldsymbol{\varepsilon}}\right) = \frac{\sum_{s=1}^{K} \dot{\gamma}_k^{(i)}\left[\dot{\boldsymbol{\varepsilon}}\left(\underline{x}\right)\right]}{\sqrt{\frac{2}{3}\dot{\boldsymbol{\varepsilon}}\left(\underline{x}\right) : \dot{\boldsymbol{\varepsilon}}\left(\underline{x}\right)}} \tag{16}$$

Noticing that $M_i\left(-\underline{x}, \dot{\boldsymbol{\varepsilon}}_B\right) = M_i\left(\underline{x}, \dot{\boldsymbol{\varepsilon}}_B\right)$, we obtain that $\left\langle M_i\left(\underline{x}, \dot{\boldsymbol{\varepsilon}}_B\right)\right\rangle_{\Omega_i} = \left\langle M_i\left(\underline{x}, \dot{\boldsymbol{\varepsilon}}_B\right)\right\rangle_{\Omega_1 \cup \Omega_2}$; therefore $\kappa \approx 0.489$ as in the case of the single crystal. It means that monocrystalline and bi-crystalline hollow spheres subjected to the hydrostatic microscopic field of Rice and Tracey (1969) have the same yield limit.

*Deviatoric point:* Under deviatoric stress $\boldsymbol{\Sigma}$ and in the limit $f \to 0$, Eq. 12 should recover the exact yield function of a pristine bi-crystal. As detailed in Appendix C, it writes:

$$\mathcal{F}^{\mathrm{bi}}_{\infty}\left(\boldsymbol{\Sigma}\right) = \left[\min_{\boldsymbol{\Delta}_\infty} \max_{s \in [\![1,K]\!]} \left\{ \frac{\left|\left(\boldsymbol{\Sigma} + \boldsymbol{\Delta}_\infty\right) : \boldsymbol{\mu}_s^{(1)}\right|}{\tau_s^{(1),\mathrm{c}}}, \frac{\left|\left(\boldsymbol{\Sigma} - \boldsymbol{\Delta}_\infty\right) : \boldsymbol{\mu}_s^{(2)}\right|}{\tau_s^{(2),\mathrm{c}}} \right\}\right]^2 - 1 \tag{17}$$

where $\boldsymbol{\Delta}_\infty$ follows the stress continuity condition at the planar interface between the two crystals, parallel to $(\underline{e}_2, \underline{e}_3)$: $\boldsymbol{\Delta}_\infty = \mathbb{E} : \boldsymbol{\Delta}_\infty$ with $\mathbb{E} = \left(\boldsymbol{I} - \underline{e}_1 \otimes \underline{e}_1\right) \overline{\otimes} \left(\boldsymbol{I} - \underline{e}_1 \otimes \underline{e}_1\right)$ and $\left[\boldsymbol{A} \overline{\otimes} \boldsymbol{B}\right]_{ijkl} = (A_{ik}B_{jl} + A_{il}B_{jk})/2$ (Dormieux and Kondo, 2010).

Having corrected the deviatoric and the hydrostatic points, the final yield surface is defined by the following Gurson-like criterion:

$$\mathcal{F}\left(\boldsymbol{\Sigma}\right) = \left[\min_{\boldsymbol{\Delta}_\infty} \max_{s \in [\![1,K]\!]} \left\{ \frac{\left|\left(\boldsymbol{\Sigma} + \boldsymbol{\Delta}_\infty\right) : \boldsymbol{\mu}_s^{(1)}\right|}{\tau_s^{(1),\mathrm{c}}}, \frac{\left|\left(\boldsymbol{\Sigma} - \boldsymbol{\Delta}_\infty\right) : \boldsymbol{\mu}_s^{(2)}\right|}{\tau_s^{(2),\mathrm{c}}} \right\}\right]^2 + 2qf\cosh\left(\kappa'\frac{\Sigma_m}{\tau^{\mathrm{c}}}\right) - 1 - (qf)^2 = 0 \tag{18}$$

When crystal 1 and crystal 2 have the same orientation, Eq. 18 reduces to the porous single crystal criterion of Paux et al. (2015) (Eq. 43), as shown in Appendix C.

### 3.3. Assessment of yield surfaces

The assessment of the proposed yield criterion (Eq. 18) is performed using the numerical homogenization results described in Section 2. Whereas the limit analysis was carried out on a hollow sphere geometry (see Fig. 5), FFT

[5] $\delta_{ij}$ stands for Kronecker delta.

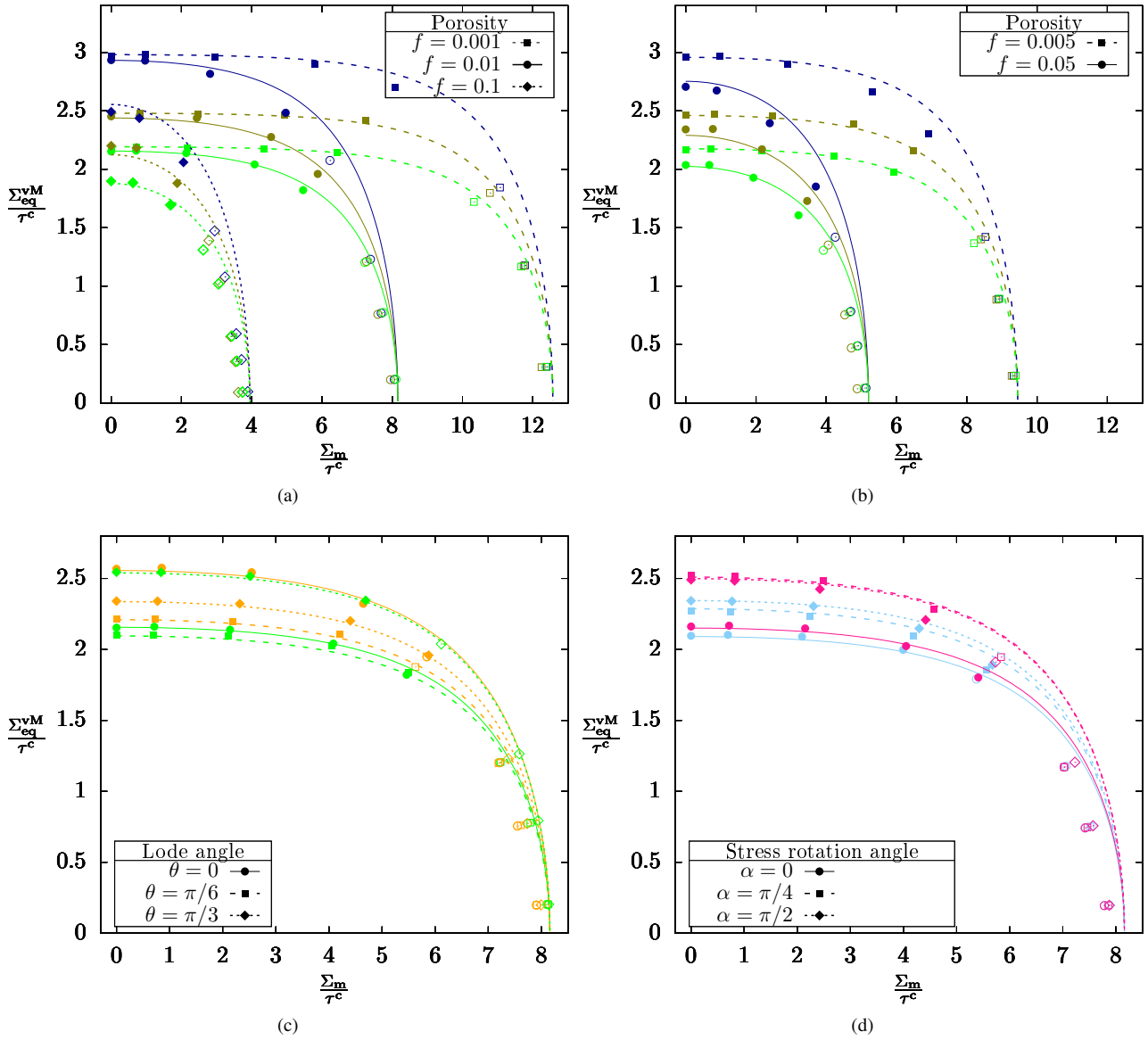


Figure 6: Comparison of yield surfaces predicted by the GTN-like criterion (lines) and unit-cell computations conducted at $n = 100$ with spherical cavities (points) : (a) porous boundary at $\theta = 0$ and porosities $f \in \{0.001, 0.01, 0.1\}$; (b) porous boundary at $\theta = 0$ and porosities $f \in \{0.005, 0.05\}$; (c) porous boundary at $f = 0.01$ and various Lode angles; (d) porous boundary at $f = 0.01$ and $\theta = 0$ with loading rotations of $\alpha$ around $\underline{e}_2$. Hollowed-out symbols mark simulations in which the deformation mode has been identified as void coalescence.

simulations could only be conducted on cuboids due to conjunction of cubic voxels and the requirement of periodic boundary conditions. As the criterion accounts for rate-independent crystals with spherical voids, only the unit-cell computations with $n = 100$ and spherical cavities are considered. As stated in the previous section, $q$ requires calibration. Following Fritzen et al. (2012), it is supposed to depend on porosity $f$. Since the competitive deformation modes known as void growth and void coalescence are accounted for by multi-yield surface plasticity, it is of paramount importance that void coalescence points are within the yield domain predicted by the void growth criterion (see Section 2.2 and Fig. 2b). Therefore, $q(f)$ is set as the maximal $q$ such as the simulations at porosity $f$, $\theta = 0$ and $\alpha = 0$ displaying void coalescence are within the yield domain and not outside. Only orientation couples that are not displayed in the graphs below were used in the calibration; therefore, the yield surfaces presented in Fig. 6 serve as validation. Fitted values of $q(f)$ are presented in Table 3; calibrated values follow the approximate relation $q(f) \approx (f + 0.005)^{-0.15}$. By comparison, $q$ have been set by previous studies on porous single crystals to 2.2 (Paux et al., 2015), 2 (Paux et al., 2018) and 1.66 (Sénac et al., 2022).

Table 3: Calibrated values of Tvergaard's parameter $q$ at various porosities $f$.

| $f$ | 0.001 | 0.005 | 0.01 | 0.05 | 0.1 | 0.2 | 0.3 |
|---|---|---|---|---|---|---|---|
| $q(f)$ | 2.14 | 1.97 | 1.85 | 1.57 | 1.45 | 1.24 | 1.17 |

Yield surfaces are shown in Fig. 6. A good agreement is observed between the GTN-like model and simulations displaying void growth. In Fig. 6a,b, it is shown that the influence of crystal orientation couples and porosity are captured well enough. In particular, the deviatoric point estimation based on the pristine bi-crystal yields excellent results for porosities $f \leq 0.01$; for higher porosities, increasing discrepancies are seen but good prediction quality is retained. In

Fig. 6c, the effect of the Lode angle $\theta$ on yield stresses is seen to be significant, especially for deviatoric loadings; this behavior is well-predicted by the model. However, some additional discussion is needed as, generally, Lode-angle effects on homogeneous yielding are believed to be two-fold:

- if the sound material has a Lode-dependent behavior, as in the case of crystals, then its influence on the yield locus of the corresponding porous material will be significant (Benallal, 2018);
- as seen in the case of von Mises matrix, homogeneous yielding of porous Lode-independent materials also display Lode-dependence that can be incorporated into models (Danas et al., 2008; Cazacu et al., 2013; Benallal et al., 2014; Leblond and Morin, 2014; Cheng et al., 2015).

In the present case, only the first contribution, which is the dominant one, is accounted for by the model. However, the second contribution, despite being negligible regarding the stress values, may significantly influence yield surface normality and thus the porosity rate (Leblond and Morin, 2014) and then the failure locus (Vishwakarma and Keralavarma, 2019). There is no reason to believe that these findings, stated for von Mises materials, may differ for crystals; nevertheless, such considerations are neglected in this work — $q$ is calibrated for $\theta = 0$ and expected to hold for other values of $\theta$ — and left for future research. Finally, in Fig. 6d, it can be inferred that the model can account for main loading axes different from $\underline{e}_1$ ($\alpha = \pi/4$ and $\pi/2$), and applied stresses with shear components ($\alpha = \pi/4$). However, since GTN-like criteria have uncoupled deviatoric and hydrostatic terms, two configurations in which the deviatoric and hydrostatic points are similar are indistinguishable by the model, as seen with orientation couple #13 (plotted in pink) loaded with $\alpha = \pi/4$ and $\pi/2$; yet, unit-cell computations clearly show that these two configurations have distinct yield stresses at intermediate triaxialities.

Due to the calibration procedure, simulations displaying void coalescence are within yield surfaces of the void growth criterion. This way, a void coalescence criterion for porous boundaries can be used simultaneously with the GTN-like model without inconsistency (see Fig. 2b).

In summary, the yield criterion presented in this section can predict satisfactorily void growth yield stresses for porous boundaries with spherical voids in the rate-independent limit. Improvement of the Gurson-like model to account for more general shapes could possibly be carried out following the lines of Monchiet et al. (2008), Keralavarma and Benzerga (2010) and Morin et al. (2015) that extended the yield locus of Benzerga and Besson (2001) to Hill materials containing spheroidal or ellipsoidal cavities.

## 4. Viscoplastic potentials for porous bi-crystals with ellipsoidal voids

In order to obtain a criterion for porous grain boundaries with ellipsoidal voids, a variational approach is adopted in the following. Indeed, variational methods provide a homogenization alternative to limit analysis that has proven fruitful for the study of voided viscoplastic single crystals (Han et al., 2013; Mbiakop et al., 2015a; Song and Ponte-Castañeda, 2017a) and polycrystals (Lebensohn et al., 2011; Nervi and Idiart, 2015; Song and Ponte Castañeda, 2018). In particular, they are expected to yield viscoplastic potentials and to be more convenient to introduce void shape effects.

In that section, pristine single crystal mechanical behavior is assumed to derive from the following viscoplastic stress potential:

$$u_n(\boldsymbol{\sigma}) = \sum_{s=1}^{K} \frac{\dot{\gamma}_0 \tau_s^c}{n+1} \left( \frac{\left| \boldsymbol{\sigma} : \boldsymbol{\mu}_s \right|}{\tau_s^c} \right)^{n+1} , \quad \dot{\boldsymbol{\varepsilon}} = \frac{\partial u_n}{\partial \boldsymbol{\sigma}} \tag{19}$$

The constitutive equation Eq. $19_b$ linking the stress potential and the plastic rate of deformation is the same as Eq. 1. Note that the Stokes-Rayleigh analogy (Hoff, 1954) enables an alternative interpretation of Eq. 19 to viscoplasticity if the strain $\boldsymbol{\varepsilon}$ is substituted to the strain rate in Eq. $19_b$: when $n = 1$ the described material has a linear elastic behavior while $n > 1$ corresponds to non-linear elasticity. This is usually the paradigm that is adopted in variational approaches (Hashin and Shtrikman, 1963; Willis, 1977; Nemat-Nasser et al., 1993).

The concept of yield surface is extended for finite $n$ by the gauge domain $\mathcal{G}$ introduced by Leblond et al. (1994):

$$\mathcal{G} = \left\{ \boldsymbol{\sigma},\ u_n(\boldsymbol{\sigma}) \leq \frac{\dot{\gamma}_0 \tau^c}{n+1} \right\} \tag{20}$$

In this convenient framework, the normality rule is kept (Benzerga and Leblond, 2010) and viscoplastic yielding is studied through the description of the gauge surface $\partial\mathcal{G}$: gauge factor $\lambda(\boldsymbol{\sigma})$ is defined as the scalar such as $\lambda(\boldsymbol{\sigma}) \cdot \boldsymbol{\sigma} \in \partial\mathcal{G}$. In the limit $n \to +\infty$, $\partial\mathcal{G}$ recovers the classical concept of yield surface.

The potential $U$ of the porous material represented by the unit-cell $\Omega$ writes:

$$U(\boldsymbol{\Sigma}) = \min_{\boldsymbol{\sigma} \in \mathcal{S}(\boldsymbol{\Sigma})} \left\langle u_n(\boldsymbol{\sigma}, \underline{x}) \right\rangle_\Omega \tag{21}$$

where $\mathcal{S}(\boldsymbol{\Sigma})$ is the set of statically admissible microscopic stress fields. Since potentials $u$ for both void and single crystals are positively homogeneous of degree $n+1$, $U$ inherits this property. Then, according to Euler's homogeneous function theorem combined with the macroscopic constitutive equation, $\boldsymbol{\Sigma} : \boldsymbol{D} = (n+1)U(\boldsymbol{\Sigma})$, enabling to compute $U$ at yielding from macroscopic tensors. Therefore, when the unit-cell is subjected to the loading described in Section 2.2, it can be obtained that:

$$\lambda\left(\boldsymbol{\Sigma}_0\right) = \left( \frac{\boldsymbol{\Sigma}_0 : \boldsymbol{D}_0}{\dot{\gamma}_0 \tau^c} \right)^{\frac{-1}{n+1}} \tag{22}$$

where $\boldsymbol{\Sigma}_0$ and $\boldsymbol{D}_0$ are the final converged values of the FFT computation. Eq. 22 is used in the post-processing of viscoplastic numerical limit-analysis of Section 2 and subsequent plotting of gauge surfaces: indeed, the numerical gauge stress is $\boldsymbol{\Sigma} = \Sigma^* (\boldsymbol{\Sigma}_0) \cdot \boldsymbol{\Sigma}_0 \in \delta\mathcal{G}$. Note that when $n \to +\infty$, Eq. 22 reduces to $\lambda (\boldsymbol{\Sigma}_0) = 1$ *i.e.* the numerical saturated stress is the sought yield stress.

### 4.1. Case $n = 1$: Hashin-Strikman estimates for periodical porous bi-crystals

The Hashin-Shtrikman bounds (Hashin and Shtrikman, 1963) on elastic moduli have been thoroughly used to study linear porous materials through the generalization of Willis (1977) who considered composites with random microstructure characterized by two-point correlation functions. Symmetries that allow analytic expressions are reviewed in Walpole (1981) and Torquato (1991). None of them are suited to the case of porous grain boundaries in which the three phases (cavity, grain 1 and grain 2) are such that cavities are always located at the interface between grains. Bi-crystals with porous boundaries have thus to be studied as periodical composites. A general framework to get bounds on elastic moduli of composites with periodical microstructure is provided by Nemat-Nasser et al. (1993) along with an explicit solution for two-phase composites. This section is devoted to obtain such a solution for three-phase composites, and that estimate will be assessed in the case of linear porous bi-crystals ($n = 1$) in Section 4.2.

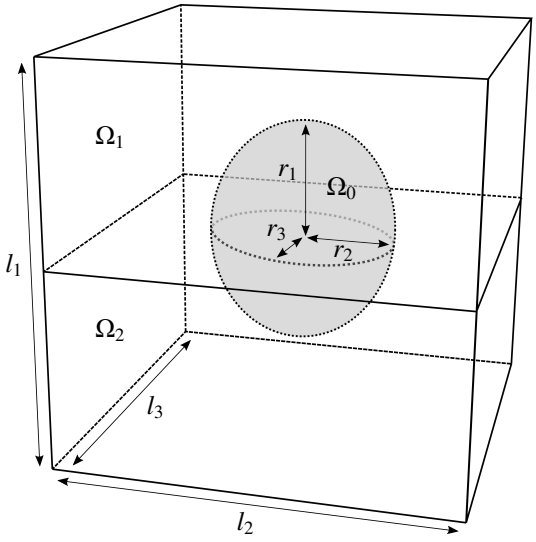


Figure 7: Rectangular prismatic unit-cell with centered ellipsoidal cavity; void axes are aligned with unit-cell axes.

We consider a three-phase periodical composite characterized by the unit-cell of Fig. 7 in which phase $i$ occupies set $\Omega_i$. $\Omega_0$ is an ellipsoid of axes $r_1$, $r_2$ and $r_3$; void aspect ratios are defined as such: $w_2 = r_1/r_2$ and $w_3 = r_1/r_3$. The volume of the unit-cell is taken as unity and volume of phase $i$ will be referred as $f_i$. Each phase $i$ is viscous linear material of pseudo-compliance[6] tensor $\mathbb{S}_i > 0$ so that $\dot{\boldsymbol{\varepsilon}} = \dot{\gamma}_0 (\mathbb{S}_i : \boldsymbol{\sigma}) / \tau^c$. According to Hashin-Strikman variational principle, every $\mathbb{S}$, rationalized as the pseudo-compliance tensor of an homogeneous comparison material, such as $\mathbb{S}_i - \mathbb{S} > 0$ (minimality condition) provide a lower bound for the macroscopic potential of the composite (Eq. 2.11 of Willis (1977) or Eq. 4.5a of Nemat-Nasser et al. (1993)):

$$U(\boldsymbol{\Sigma}) \geq \frac{\dot{\gamma}_0 \tau^c}{2} \boldsymbol{\Sigma} : \overline{\mathbb{S}} : \boldsymbol{\Sigma} \quad \text{with} \quad \overline{\mathbb{S}} = \mathbb{S} + \sum_{i=0}^{2} f_i \mathbb{S}^{(i)} \tag{23}$$

According to Nemat-Nasser et al. (1993), tensors $\mathbb{S}^{(i)}$ are given by the following linear system within the space of symmetric fourth-order tensors:

$$\forall i \in [\![0, 2]\!], \ (\mathbb{S}_i - \mathbb{S})^{-1} : \mathbb{S}^{(i)} + \sum_{j=0}^{2} f_j \, \mathbb{A}_{ij} : \mathbb{S}^{(j)} - \mathbb{I} = 0 \tag{24}$$

where correlation tensors (or Eshelby sums) $\mathbb{A}_{ij}$ account for the interactions between phases and thus hold the microstructure information of the linear composite:

$$\mathbb{A}_{ij}(\mathbb{S}) = \sum_{\substack{\underline{\xi} = (2n_1\pi/l_1, 2n_2\pi/l_2, 2n_3\pi/l_3) \\ (n_1,n_2,n_3) \in (\mathbb{Z}^3)^*}} \mathrm{Re}\left[ g_i\left(\underline{\xi}\right) g_j\left(-\underline{\xi}\right) \right] \underbrace{\left( \mathbb{S}^{-1} - \mathbb{S}^{-1} : \mathrm{sym}\left[ \underline{\xi} \otimes (\underline{\xi} \cdot \mathbb{S}^{-1} \cdot \underline{\xi})^{-1} \otimes \underline{\xi} \right] : \mathbb{S}^{-1} \right)}_{\mathbb{A}\left(\underline{\xi}, \mathbb{S}\right)} \tag{25}$$

$$\text{with} \quad g_j\left(\underline{\xi}\right) = \frac{1}{f_j} \int_{\underline{x} \in \Omega_j} e^{i \underline{\xi} \cdot \underline{x}} \tag{26}$$

where $g_i$ is the Fourier transform of the characteristic function of $\Omega_i$. Eq. 25 differs from Nemat-Nasser et al. (1993) in that only the real part of $\mathbb{A}_{ij}$ is considered. Indeed, it is safely assumed that components of $\mathbb{S}^{(i)}$ are real-valued, allowing

[6] This terminology is motivated by Stokes-Rayleigh analogy.

to focus attention on the real part of Eq. 24. For conciseness, expressions of $g$-functions are provided in Appendix D for ellipsoidal cavities as well as elliptic-cylindrical cavities. However, explicit forms are not necessary to verify the following relations:

$$\begin{aligned} \mathbb{A}_{01} = \mathbb{A}_{02}\,, \quad \forall (i,j) \in [\![0,2]\!]^2,\ \mathbb{A}_{ij} = \mathbb{A}_{ji} \\ \mathbb{A}_{11} = \mathbb{A}_{22}\,, \quad f\mathbb{A}_{00} + (1-f)\mathbb{A}_{01} = 0 \\ f\mathbb{A}_{01} + \tfrac{1}{2}(1-f)\mathbb{A}_{11} + \tfrac{1}{2}(1-f)\mathbb{A}_{12} = 0 \end{aligned} \tag{27}$$

the last two deriving from the fact that $f_0 g_0 + f_1 g_1 + f_2 g_2 = 0$. Eq. 27 implies that all correlation tensors can be expressed from $\mathbb{A}_{01}$ and $\mathbb{A}_{12}$. In order to solve the set of Eqs. 24, it is convenient to introduce tensors $\mathbb{B}_i$:

$$\forall i \in [\![0,2]\!],\ \mathbb{B}_i = \frac{f}{2}\mathbb{A}_{01} + \frac{1-f}{2}\mathbb{A}_{12} - (\mathbb{S}_i - \mathbb{S})^{-1} \tag{28}$$

Non-commutative algebra finally yield the following expressions:

$$\begin{aligned} \mathbb{S}^{(0)} &= -\frac{1}{1-f}\left\{\mathbb{A}_{01}^{-1} + \frac{1}{2}\left[\left(\mathbb{B}_1 - \mathbb{B}_0\mathbb{B}_2^{-1}\mathbb{B}_0\right)^{-1}\left(\mathbb{I} + \mathbb{B}_0\mathbb{B}_2^{-1}\right) + \left(\mathbb{B}_2 - \mathbb{B}_0\mathbb{B}_1^{-1}\mathbb{B}_0\right)^{-1}\left(\mathbb{I} + \mathbb{B}_0\mathbb{B}_1^{-1}\right)\right]\right\} \\ \mathbb{S}^{(1)} &= -\frac{1}{1-f}\left(\mathbb{B}_1 - \mathbb{B}_0\mathbb{B}_2^{-1}\mathbb{B}_0\right)^{-1}\left(\mathbb{I} + \mathbb{B}_0\mathbb{B}_2^{-1}\right) \\ \mathbb{S}^{(2)} &= -\frac{1}{1-f}\left(\mathbb{B}_2 - \mathbb{B}_0\mathbb{B}_1^{-1}\mathbb{B}_0\right)^{-1}\left(\mathbb{I} + \mathbb{B}_0\mathbb{B}_1^{-1}\right) \end{aligned} \tag{29}$$

In the case of the porous linear bi-crystal, $\mathbb{S}_0 = \infty$ and $\mathbb{S}_1$ and $\mathbb{S}_2$ are given by Eq. 14, corrected by a parameter $\kappa \to +\infty$ to regain inversibility:

$$\mathbb{S}_i = \sum_{s=1}^{K} \frac{1}{\left(\tau_s^{(i),c}\right)^2}\left[\boldsymbol{\mu}_s^{(i)} \otimes \boldsymbol{\mu}_s^{(i)}\right] + \frac{1}{\left(\tau^{(i),c}\right)^2}\frac{1}{3\kappa}\mathbb{J} \tag{30}$$

Since no obvious choice of $\mathbb{S}$ respecting the minimality condition exists, this condition is dropped and the homogeneous material is chosen to be the pristine bi-crystal: $\mathbb{S}$ is given by Eq. C.4. The left-hand expression of Eq. 23 thus loses its bounding character and becomes an estimate of $U(\boldsymbol{\Sigma})$. Some degenerate cases are worth commenting. On the one hand, when grain 1 and grain 2 have the same crystal orientation, $\mathbb{S} = \mathbb{S}_1 = \mathbb{S}_2$ and the modulus estimate reduces to:

$$\overline{\mathbb{S}} = \mathbb{S}_1 + \mathbb{A}_{00}\,(\mathbb{S}_1)^{-1} \tag{31}$$

which was already presented by Nemat-Nasser et al. (1993) (Eq. 6.5a). This approximated modulus is the periodical twin to the expression given by Willis (1977) (Eq. 3.16) in the context of random cavities and involving Eshelby inclusion integral:

$$\overline{\mathbb{S}} = \mathbb{S}_1 + \frac{f}{1-f}\left[\left\langle \mathbb{A}\left(\underline{\xi}, \mathbb{S}_1\right)\right\rangle_{\partial\Omega_0}\right]^{-1} \tag{32}$$

The absence of factor $f/(1-f)$ in Eq. 31 may seem surprising, but it is simply hidden in $\mathbb{A}_{00}$ as will be shown in Appendix E. On the other hand, when $f \to 0$, $\mathbb{A}_{12} \to -\mathbb{A}\left(\underline{e}_1, \mathbb{S}\right)$. Changing gear to $\mathbb{S} = \mathbb{S}_1$, the approximated pseudo-compliance becomes:

$$\overline{\mathbb{S}} = \mathbb{S}_1 + \left[2\,(\mathbb{S}_2 - \mathbb{S}_1)^{-1} + \mathbb{A}\left(\underline{e}_1, \mathbb{S}_1\right)\right]^{-1} \tag{33}$$

which is the result of Francfort and Murat (1986) (see Norris (1990) for a simplified presentation) for a pristine laminate. A similar agreement is found choosing $\mathbb{S} = \mathbb{S}_2$. Therefore, setting $\mathbb{S}$ according to Eq. C.4 (or equivalently Eq. 33) may yield $\overline{\mathbb{S}} = \mathbb{S}$; due to the intricate expressions it was not possible to derive equality but this conjecture was at least checked numerically on a few examples. In summary, the expressions are consistent in both extreme cases of pristine bi-crystals and porous single crystals.

### 4.2. *Case $n = 1$: Assessment of gauge surfaces*

In the previous section, a complete set of equations gives an estimate for the pseudo-compliance of the linear porous bi-crystal and therefore an approximate for its potential. Analytical gauge surfaces are determined by the conjunction of Eq. 23 and Eq. 20:

$$\boldsymbol{\Sigma} \in \partial\mathcal{G} \quad \Leftrightarrow \quad \boldsymbol{\Sigma} : \overline{\mathbb{S}} : \boldsymbol{\Sigma} = 1 \tag{34}$$

$\kappa = 10^6$ is chosen in Eq. 30, as higher values may cause instabilities when inverting tensors. $\mathbb{A}_{ij}$ series (Eq. 27) are truncated from $(n_1, n_2, n_3) \in \left(\mathbb{Z}^3\right)^*$ to $\left([\![-100, 100]\!]^3\right)^*$ to ensure maximal accuracy; fewer terms would also lead to satisfying estimates, but such an investigation is outside the scope of this study. In order to assess this model, gauge surfaces are plotted in Fig 8 and compared to numerical surfaces obtained using Eq. 22 on unit-cell simulations.

As seen in Fig. 8a, the estimates achieve very satisfying precision: variations of gauge stress according to crystal orientations are perfectly accounted for, while the softening effect of porosity is correctly predicted in a wide range of $f$

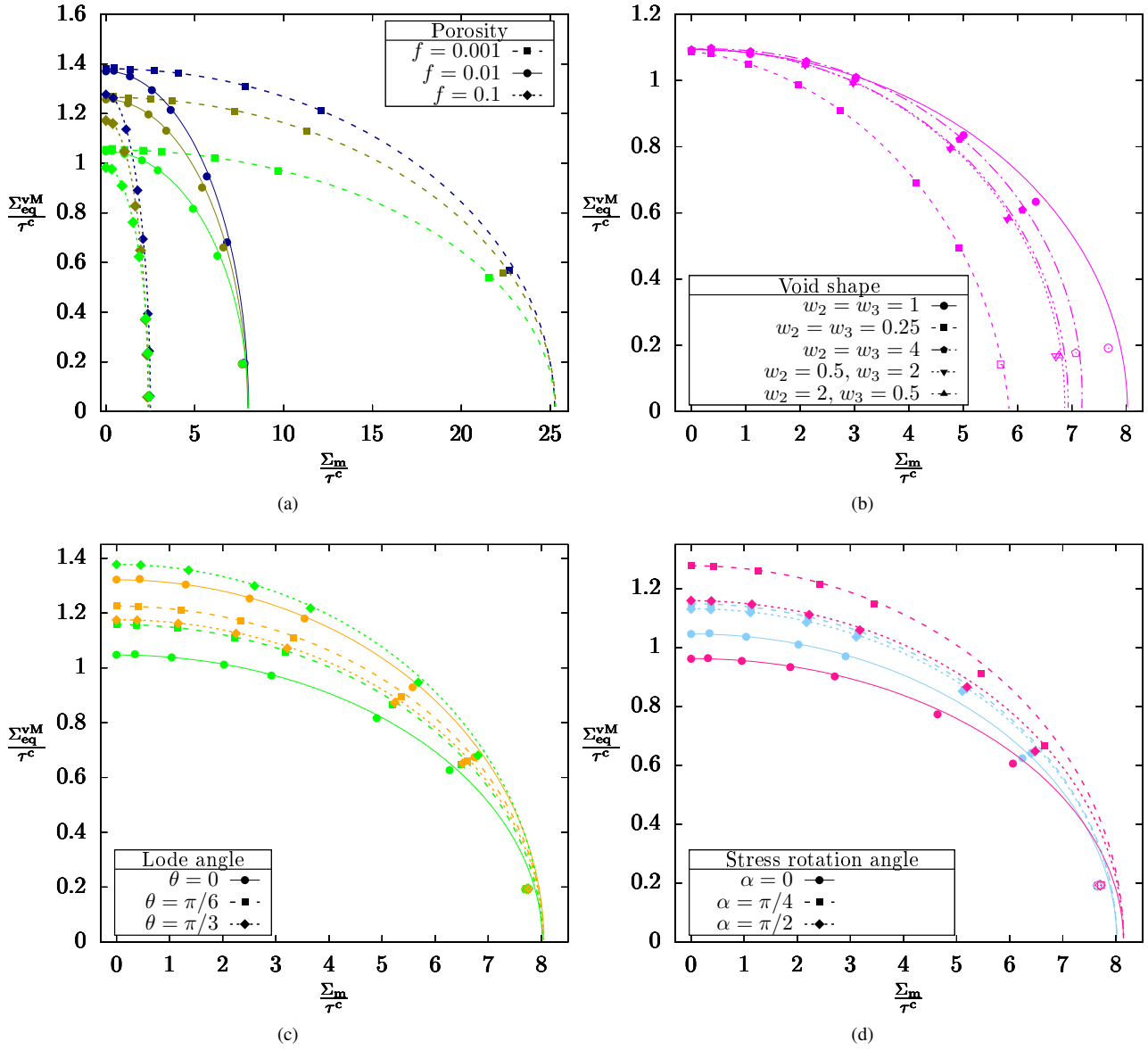


Figure 8: Comparison of gauge surfaces predicted by variational estimates (lines) and unit-cell computations (points) at $n = 1$: (a) porous boundary at $\theta = 0$ and various spherical porosities; (b) porous boundary at $f = 0.01$ and $\theta = 0$ with ellipsoidal cavities of various shapes; (c) porous boundary with spherical cavity at $f = 0.01$ and various Lode angles; (d) porous boundary with spherical cavity at $f = 0.01$ and $\theta = 0$ with loading rotations of $\alpha$ around $\underline{e}_2$. Hollowed-out symbols mark simulations in which the deformation mode has been identified as void coalescence.

(in fact for all the values considered in the unit-cell database: *i.e* from $f = 0.001$ to $f = 0.3$). As in the case of single crystals, it can be noticed that porosity has a greater effect on the hydrostatic point than on the deviatoric point. Fig. 8b assesses the impact of void shape; again, it is underlined that the proposed estimates are in agreement with unit-cell computations for all ellipsoidal geometries considered. For a given porosity, oblate cavities in the plane $(\underline{e}_2, \underline{e}_3)$ are found more damaging than prolate cavities, both of them displaying softer behavior than spherical cavities. Ellipsoidal cavities with $w_2 = 0.5$ and $w_3 = 2$ (and *vice-versa*) have intermediate gauge stresses between the two spheroidal void geometries. Lode angle influence is shown in Fig. 8c: as in the case of single crystals (Paux et al., 2018), no general rule can be stated on the angle $\theta_{\max}$ at which the maximum yield stress is reached. Orientations displayed on the graph were chosen because of the important effect of $\theta$, but for other orientations this influence was noticed to be less important. All these trends are quantitatively reflected in the model. All these findings do not depend on crystallographic orientations as they were seen on all couples present in the database. Finally, stress rotations were investigated in Fig. 8d: $\alpha = \pi/2$ is a loading whose principal stress axis is along $\underline{e}_3$ while $\alpha = \pi/4$ have shear components since the main loading axis is along $\underline{e}_1 + \underline{e}_3$. Due to the complex interplay between loading directions and crystallographic orientations, the effect of $\alpha$ vary greatly according to the grain boundary that is considered. This is in contradiction with the findings of Wen and Yue (2007), Zhang et al. (2008) and Liu et al. (2009) who considered too few orientation couples to notice their influence. This conclusion will be seen to hold for other values of $n$ (see Section 4.4).

As explained in Appendix B, void coalescence was identified in a handful of simulations (see Fig 8b,c,d). Although the predictions of the model are not too far from these points, they are the computations where the discrepancy is the highest. Such a finding is no surprise as the derivation conducted in the previous section is only supposed to account for voided boundaries where plasticity is diffuse.

### 4.3. Case $n > 1$: Heuristical variational extension

Variational methods of non-linear composite homogenization based on linear comparison materials have been widely used; see Castañeda and Suquet (1997) for a synthesis. In the aforementioned framework, the shear stresses on slip systems $s$ are supposed to be homogeneous in each crystal $i$, *i.e.* $\tau_s^{(i)}\left(\underline{x}\right) = \overline{\tau}_s^{(i)}$. Injecting this hypothesis in Eq. 21 means that the homogenized potential of a porous polycrystal of $M$ grains (Song and Ponte-Castañeda, 2017a; Song and Ponte Castañeda, 2018) is sought in the form:

$$U^{\mathrm{LC}}(\boldsymbol{\Sigma}) = \sum_{i=1}^{M} f_i \left[ \sum_{s=1}^{K} \frac{\dot{\gamma}_0 \tau_s^{(i),\mathrm{c}}}{n+1} \left( \frac{\overline{\tau}_s^{(i)}}{\tau_s^{(i),\mathrm{c}}} \right)^{n+1} \right] \tag{35}$$

In our study, only the cases $M = 1$ and $M = 2$ shall be considered. Note that there is $M + 1$ phases due to the presence of a cavity of volume fraction $f_0 = f$, but the corresponding term does not appear in Eq. 35 since the local stress potential of the void is 0. When $M = 1$, $f_1 = 1 - f$ and when $M = 2$, $f_1 = f_2 = (1 - f)/2$. The homogenized resolved shear stresses $\overline{\tau}_s^{(i)}$ should be chosen in order to minimize the macroscopic potential and to fulfill the stress admissibility conditions. In linear comparison methods, $\left(\overline{\tau}_s^{(i)}\right)$ are solutions of a set of non-linear equations in which the pseudo-compliance $\overline{\mathbb{S}}$ of a well-chosen porous linear comparison material intervenes. Determining $U$ require solving a set of $m \times M \times K$ non-linear equations — integer $m$ is contingent on the exact linear comparison method (*e.g.* variational method, second-order method). Therefore, Eq. 35 is not analytic and may be too computationally expensive to implement in numerical simulations of ductile fracture, prompting the development of simpler expressions. In the case $M = 1$, Mbiakop et al. (2015a) has suggested the following analytic form for $\left(\overline{\tau}_s^{(i)}\right)$:

$$\overline{\tau}_s^{(i)} = \frac{1}{1-f} \sqrt{\left(\tau_s^{(i)}\right)^2 + \boldsymbol{\Sigma} : \left[\mathbb{A} + (q_J(n,f)^2 - 1)\, \mathbb{J} : \mathbb{A} : \mathbb{J}\right] : \boldsymbol{\Sigma}} \quad \text{with} \quad \mathbb{A} = \frac{(\tau^{\mathrm{c}})^2}{K} \left[(1-f)\overline{\mathbb{S}} - \mathbb{S}\right] \tag{36}$$

where $\tau_s^{(i)}$ is the resolved shear stress of the pristine crystal, $\mathbb{A}$ is linked to the pseudo-compliance $\overline{\mathbb{S}}$ of the linear porous crystal and $q_J$ is a scalar depending on $n$ and $f$. Since the work of Mbiakop et al. (2015a) focused on single crystal with random cavities, $\tau_s^{(i)} = \boldsymbol{\mu}_s : \boldsymbol{\Sigma}$, $\mathbb{S}$ is set by Eq. $14_b$ and $\overline{\mathbb{S}}$ is set by Eq. 32. The substitution of Eq. 36 into Eq. 35 thus yields:

$$U^{\mathrm{LC}}_{\mathrm{mono}}(\boldsymbol{\Sigma}) = \frac{1}{(1-f)^n} \sum_{s=1}^{K} \frac{\dot{\gamma}_0 \tau_s^{\mathrm{c}}}{n+1} \left[ \frac{\sqrt{\boldsymbol{\Sigma} : (\boldsymbol{\mu}_s \otimes \boldsymbol{\mu}_s + \mathbb{A} + (q_J(n,f)^2 - 1)\, \mathbb{J} : \mathbb{A} : \mathbb{J}) : \boldsymbol{\Sigma}}}{\tau_s^{\mathrm{c}}} \right]^{n+1} \tag{37}$$

which is exactly Eq. 40 of Mbiakop et al. (2015a). In the limit where $f$ goes to 0, $\mathbb{A} = 0$ so this expression reduces to the pristine single crystal potential (Eq. 19). When $n = 1$, if $q_J(1, f)$ is taken equal to 1 then Eq. 37 reduces to the Hashin-Strikman estimate for linear porous single crystal (Eq. $23_a$ with $\overline{\mathbb{S}}$ given by Eq. 32):

$$U^{\mathrm{LC}}_{\mathrm{mono}}(\boldsymbol{\Sigma}) = \frac{\dot{\gamma}_0 \tau^{\mathrm{c}}}{2(1-f)} \left[ \boldsymbol{\Sigma} : \left( \frac{K}{(\tau^{\mathrm{c}})^2} \mathbb{A} \right) : \boldsymbol{\Sigma} + \sum_{s=1}^{K} \boldsymbol{\Sigma} : \left( \frac{1}{(\tau_s^{\mathrm{c}})^2} \boldsymbol{\mu}_s \otimes \boldsymbol{\mu}_s \right) : \boldsymbol{\Sigma} \right] = \frac{\gamma_0 \tau^{\mathrm{c}}}{2} \boldsymbol{\Sigma} : \overline{\mathbb{S}} : \boldsymbol{\Sigma} \tag{38}$$

Therefore, the expression of Mbiakop et al. (2015a) exhibits satisfying behavior in the limiting cases of a linear porous single crystal and a pristine non-linear single crystal. Next, Eq. 36 is applied to the porous bicrystal case ($M = 2$). From Appendix C, it is obtained that $\tau_s^{(i)} = \boldsymbol{\mu}_s^{(i)} : \left(\boldsymbol{\Sigma} \pm \widetilde{\boldsymbol{\Delta}_n}(\boldsymbol{\Sigma})\right)$ with $\widetilde{\boldsymbol{\Delta}_n}$ defined in Eq. C.2. As in Section 4.1, $\mathbb{S}$ is set by Eq. 33 (or equivalently Eq. C.4) and $\overline{\mathbb{S}}$ is set by Eq. $23_b$. Therefore, substitution of Eq. 36 into Eq. 35 yields:

$$U^{\mathrm{LC}}_{\mathrm{bi}}(\boldsymbol{\Sigma}) = \frac{1}{2(1-f)^n} \sum_{i=1}^{2} \sum_{s=1}^{K} \frac{\dot{\gamma}_0 \tau_s^{(i),\mathrm{c}}}{n+1} \left[ \frac{\sqrt{\left(\boldsymbol{\mu}_s^{(i)} : \left(\boldsymbol{\Sigma} \pm \widetilde{\boldsymbol{\Delta}_n}\right)\right)^2 + \boldsymbol{\Sigma} : (\mathbb{A} + (q_J(n,f)^2 - 1)\, \mathbb{J} : \mathbb{A} : \mathbb{J}) : \boldsymbol{\Sigma}}}{\tau_s^{(i),\mathrm{c}}} \right]^{n+1} \tag{39}$$

In the limit where $f$ goes to 0, $\mathbb{A} = 0$ so this expression reduces to the crystalline laminate potential (Eq. C.2). When $n = 1$ and $q_J(1, f)$ is taken equal to 1, Eq. 39 recovers the Hashin-Strikman estimate for the linear porous bi-crystal (Eq. 23):

$$\begin{aligned} U^{\mathrm{LC}}_{\mathrm{bi}}(\boldsymbol{\Sigma}) &= \frac{\dot{\gamma}_0 \tau^{\mathrm{c}}}{2(1-f)} \left[ \boldsymbol{\Sigma} : \left( \frac{K}{(\tau^{\mathrm{c}})^2} \mathbb{A} \right) : \boldsymbol{\Sigma} + \frac{1}{2} \sum_{s=1}^{K} \left( \frac{\boldsymbol{\mu}_s^{(1)} : \left(\boldsymbol{\Sigma} + \widetilde{\boldsymbol{\Delta}_1}\right)}{\tau_s^{(1),\mathrm{c}}} \right)^2 + \left( \frac{\boldsymbol{\mu}_s^{(2)} : \left(\boldsymbol{\Sigma} - \widetilde{\boldsymbol{\Delta}_1}\right)}{\tau_s^{(2),\mathrm{c}}} \right)^2 \right] \\ &= \frac{\dot{\gamma}_0 \tau^{\mathrm{c}}}{2(1-f)} \left[ \boldsymbol{\Sigma} : \left( (1-f)\overline{\mathbb{S}} - \mathbb{S} \right) : \boldsymbol{\Sigma} + \boldsymbol{\Sigma} : \mathbb{S} : \boldsymbol{\Sigma} \right] \quad \text{(see Eq. C.4)} \\ &= \frac{\dot{\gamma}_0 \tau^{\mathrm{c}}}{2} \boldsymbol{\Sigma} : \overline{\mathbb{S}} : \boldsymbol{\Sigma} \end{aligned} \tag{40}$$

Therefore, the heuristic homogenized potential proposed here (Eq. 39) is coherent with previous results in the limiting cases of a linear porous bi-crystal and a non-linear pristine bi-crystal. Until now, the value of $q_J$ was not discussed and supposed to be 1. In that case, use of Eq. 37 and Eq. 39 to predict gauge surfaces reveal that estimated potential are too small at high trixialities, as is usually the case with variational estimates. $q_J$ could be chosen to recover exact results for the hydrotatic behavior of porous crystals but unfortunately no such result is known. Instead, following Mbiakop

et al. (2015a), the limiting case of crystals with an infinite number of equiangular equivalent slip systems ($K \to +\infty$ and $\tau_s^{(i),c} = \tau^c$) and spherical voids is considered and $q_J$ is fixed so that this behavior is correctly predicted under pure hydrostatic loading. It is shown in Appendix E that this coherency condition writes:

$$q_J(n,f) = a\overline{g}_n \sqrt{\frac{20}{3f}} \left( \frac{1-f}{n(f^{-1/n}-1)} \right)^{\frac{n}{n+1}} \tag{41}$$

where $a = 3/2$ for spherical voids and $\overline{g}_n$ is a constant that only depend on $n$. Note that:

$$q_J(1,f) = 1 \;\Leftrightarrow\; \overline{g}_1 = \frac{1}{a}\sqrt{\frac{3}{20}} \tag{42}$$

Eq. 41 can be qualitatively related to the hydrostatic behavior of Gurson-type yield criteria (see Paux et al. (2015) and Eq. 18): under pure hydrostatic loading, the dependence on crystallographic orientations is thought to vanish, at least at the first order.

In summary, the heuristic variational model developed for viscoplastic bi-crystals with ellipsoidal voids is constituted by the conjunction of Eqs. 39 and 41.

### 4.4. *Case $n > 1$: Assessment of gauge surfaces*

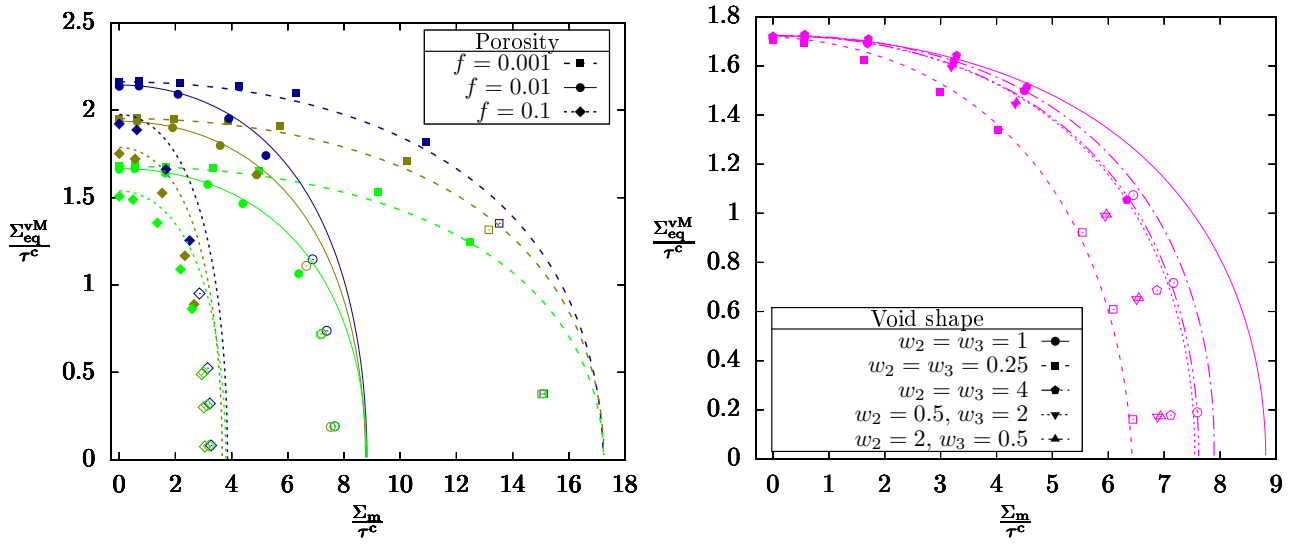


(a) (b)

Figure 9: Comparison of gauge surfaces predicted by variational estimates (lines) and unit-cell computations (points) at $n = 3$: (a) porous boundary at $\theta = 0$ and various spherical porosities; (b) porous boundary at $f = 0.01$ and $\theta = 0$ with ellipsoidal cavities of various shapes. Hollowed-out symbols mark simulations in which the deformation mode has been identified as void coalescence.

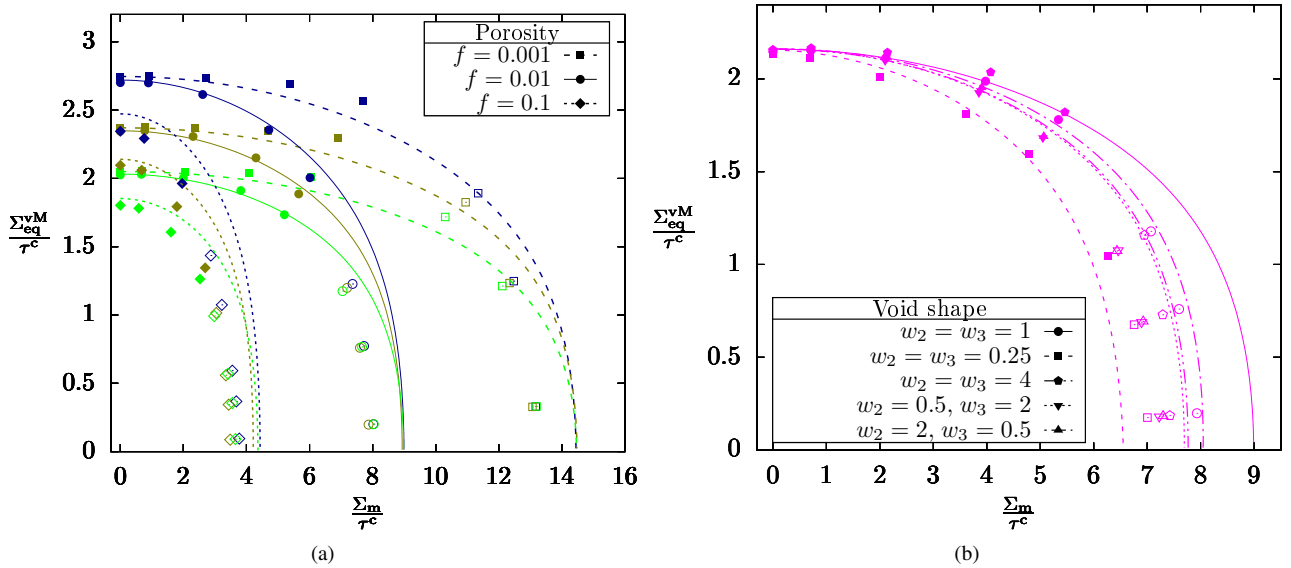


(a) (b)

Figure 10: Comparison of gauge surfaces predicted by variational estimates (lines) and unit-cell computations (points) at $n = 10$: (a) porous boundary at $\theta = 0$ and various spherical porosities; (b) porous boundary at $f = 0.01$ and $\theta = 0$ with ellipsoidal cavities of various shapes. Hollowed-out symbols mark simulations in which the deformation mode has been identified as void coalescence.

Before carrying assessment of gauge surfaces, some additional discussion on $\overline{g}_n$ is needed. In Mbiakop et al. (2015a) as well as in Appendix E, an approximate argument based on a study of porous materials with Lode-dependent yield criteria (Benallal, 2018) lead to Eq. E.21, which gives an explicit value for $\overline{g}_n$. Values from Eq. E.21 and those given in Mbiakop et al. (2015a) are compared in Table 4: they are very close for $n \in [\![1, 10]\!]$ but quite distinct[7] for $n = 100$. Unfortunately, when $n > 1$, using the value of $\overline{g}_n$ given by Eq. E.21 to predict gauge surfaces lead to gauge stresses at high triaxiality ratios that are significantly below the numerical gauge stresses provided by unit-cell simulations. For that reason, Eq. E.21 is discarded and $\overline{g}_n$ is set as a calibration parameter for $n > 1$. Note that the approximate nature of Eq. E.21 allow for such emancipation (see Appendix E). For a given $n$, $\overline{g}_n$ is chosen to minimize the mean square error in the prediction of gauge surfaces for porous boundaries with spherical voids and subjected to loadings with $\theta = 0$ and $\alpha = 0$. Only simulations which display void growth were considered; values obtained through this optimization procedure are reported in Table 4 and shall be used in the graphs shown hereafter.

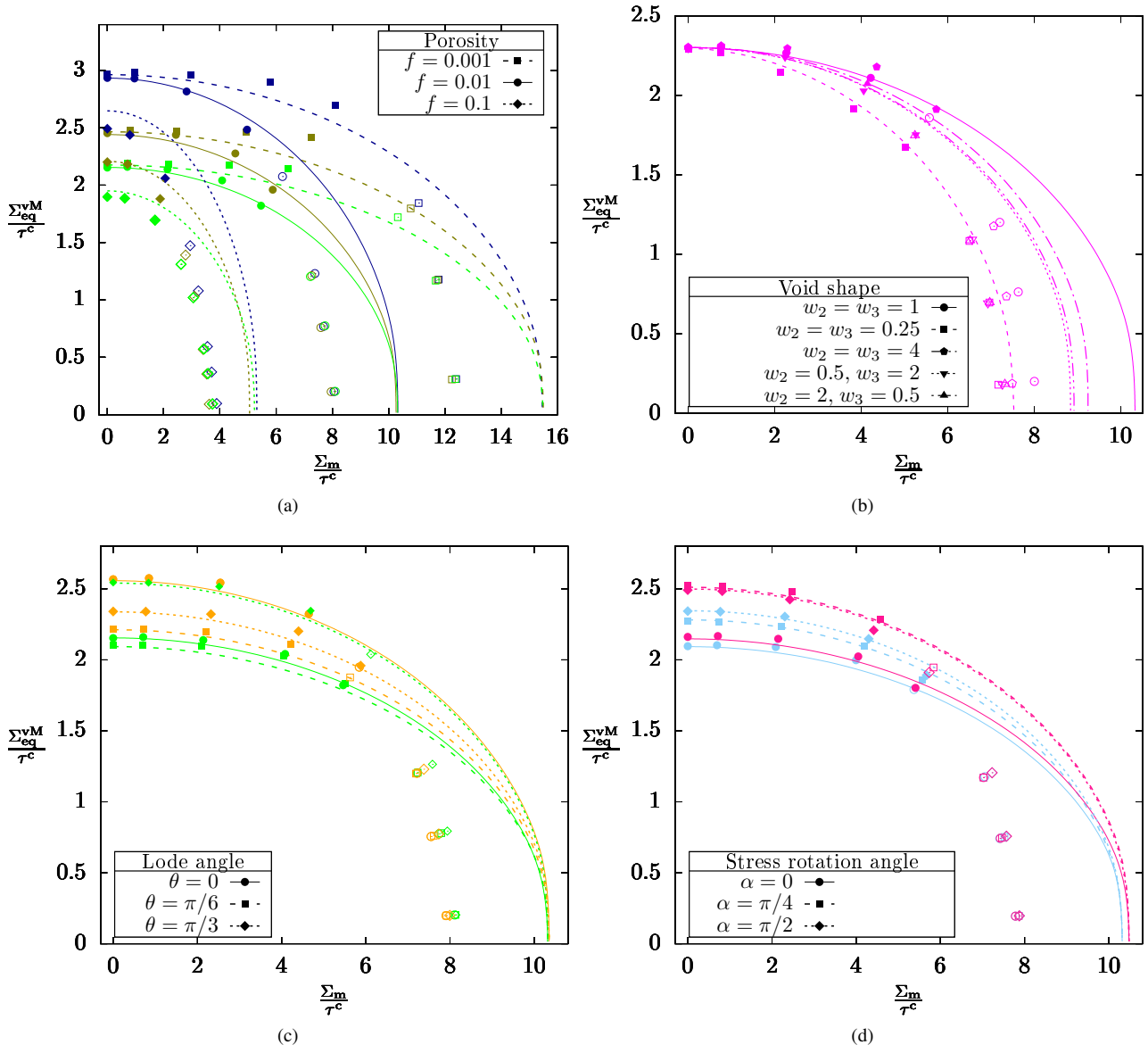


Figure 11: Comparison of gauge surfaces predicted by variational estimates (lines) and unit-cell computations (points) at $n = 100$: (a) porous boundary at $\theta = 0$ and various spherical porosities; (b) porous boundary at $f = 0.01$ and $\theta = 0$ with ellipsoidal cavities of various shapes; (c) porous boundary with spherical cavity at $f = 0.01$ and various Lode angles; (d) porous boundary with spherical cavity at $f = 0.01$ and $\theta = 0$ with loading rotations of $\alpha$ around $\underline{e}_2$. Hollowed-out symbols mark simulations in which the deformation mode has been identified as void coalescence.

In order to assess the heuristical extension presented in the previous section, gauge surfaces for $n = 3$, $n = 10$ and $n = 100$ are respectively shown in Fig. 9, Fig. 10 and Fig. 11. Even if the predictions are satisfying on the range of $n$ considered, it can be seen that agreement diminishes when $n$ increases. This was expected since the rigorous estimate was only obtained for $n = 1$ and further extension to $n > 1$ is likely to become cruder as non-linearity grows. Thus, Fig. 9 ($n = 3$) displays a better agreement than Fig. 10 ($n = 10$) which itself shows better predictions than Fig. 11 ($n = 100$). Nevertheless, the variational model at $n = 100$ compares well with the Gurson-like locus (Fig 6). For all values of $n$, the combined effects of porosity and crystal orientation couples are well predicted (Figs. 9-11a), as well as the influence of

[7] This is no surprise since Mbiakop et al. (2015a) computed $\overline{g}_n$ for $n \in [\![1, 10]\!]$ from a formula akin to Eq. E.21 (although not explicitly given) and then extrapolated the numerical trend found in that interval to obtain $\overline{g}_{100}$.

Table 4: Values of $\overline{g}_n$ obtained by various methods.

| $n$ | | 1 | 3 | 10 | 100 |
|---|---|---|---|---|---|
| $\overline{g}_n$ | Theoretical (Eq. E.9$_b$) | 0.26 | 0.31 | 0.39 | 0.48 |
| | Mbiakop et al. (2015a) | 0.26 | 0.32 | 0.38 | 0.40 |
| | Calibration | 0.26 | 0.26 | 0.31 | 0.31 |

Lode angle and principal axes, which are only shown in the more challenging case ($n = 100$, see Fig. 11c,d) for brevity. From these assessments, it can be inferred that gauge surfaces are correctly predicted for arbitrary loading configurations and that the model is fit for use in finite-element simulations. Furthermore, the results for ellipsoidal cavities presented in Figs. 9-11b are quite satisfying as far as the void growth stage is concerned. The effect of oblate cavities along the grain boundary ($w_2 = w_3 = 0.25$) is particularly well predicted. The only disappointment come from the asymmetry of the gauge surface for prolate cavities ($w_2 = w_3 = 4.0$) that is insufficiently marked in the model predictions, a discrepancy that increases with $n$ and make prolate cavities detrimental to material strength (similarly to the case $n = 1$, from which the heuristical extension is drawn) whereas they are beneficial to it. It can be seen in Mbiakop et al. (2015a) that the introduction of an additional parameter $\alpha_2$ increased the influence of the microstructural tensor $\mathbb{A}$ on resolved shear stresses (Eq. 36), enabling the reproduction of such effects at the cost of additional calibration.

It can be seen that increasing $n$ foster void coalescence (see also Fig. 8), so that smaller sections of gauge surfaces belongs to void growth stage. A sharp transition can be seen (especially at $n = 100$) in the surfaces obtained by numerical homogenization: a first section with a high curvature at low triaxialities is supplemented by a straight-lined section at high triaxialities. This finding justifies the choice to model gauge surfaces with a multi-surface criterion (*e.g.* Keralavarma (2017)), only the void growth criterion being discussed here. This contrasts with other studies in which a unique yield criteria obtained in the dilute porosity regime is expected to account for all possible deformation modes: in Lebensohn et al. (2011), the estimations presented are naturally too stiff near the hydrostatic point due to the neglect of plastic localization, whereas the model presented in Mbiakop et al. (2015a) and Mbiakop et al. (2015b) displays degraded agreement at intermediate triaxialities in an effort to recover the hydrostatic point; remark that additional calibration parameters $\alpha_1$ and $\alpha_2$ that were needed at $n = 100$ (Mbiakop et al., 2015a) are not used here.

Finally, it is noted that the effect of choosing square periodicity of cavities in the plane $(\underline{e}_2, \underline{e}_3)$ has not been evaluated, but is believed to be minor given the fact that interactions between cavities are weak in the void growth stage. Nevertheless, Hashin-Strikman estimates for porous bi-crystals with planar randomness of cavities may be achieved by combining the derivations of Willis (1977) and Nemat-Nasser et al. (1993).

Even if it is not in the scope of this study, some considerations on computational efficiency may be stated. The GTN-like yield criterion is quite efficient provided that the value of $\mathbf{\Delta}_\infty$ is known. Since the normalized value of this tensor only depends on the Lode angle and stress principal axes that may evolve slowly in ductile fracture simulations, optimization of Eq. C.2 will not be needed at every time step. Alternatively, the use of a surrogate model for $\mathbf{\Delta}_\infty$ would also accelerate simulations. Variational estimates (Eq. 36) are more computation intensive with the determination of both $\overline{\mathbb{S}}$ and $\mathbf{\Delta}_n$, the latter being negligible compared to the former. Since $\overline{\mathbb{S}}$ only depends on porosity and void shape, its updates can be reduced to significant geometric evolutions, and accelerated by determining an optimal truncation for series $\mathbb{A}_{01}$ and $\mathbb{A}_{12}$ (Eq. 25). It is also worthy to note that computations can be alleviated by using a surrogate model for $g_1$ (Eq. D.4) or by considering elliptic-cylindrical voids for which function $g_1$ possesses a closed-form (see Appendix D).

## 5. Application to the competition between intergranular and transgranular void growth

The yield criteria proposed in the previous sections allow for a discussion of the competition between transgranular and intergranular ductile fracture. Since polycrystal ductile failure is an intricate phenomenon in which work hardening, texture evolution and strain localization play an important role, definitive predictions of the dominant fracture mechanism are outside the scope of this study. However, the two criteria derived in this study can predict, given a microstructure with pre-existing cavities and a loading state, the location — grain interiors or grain boundaries — where void growth will first occur.

As a first work example, let us consider a porous bi-crystal with a random distribution of spherical cavities, both at the grain boundary and within the grains, corresponding to the microstructure shown in Fig. 12. Constant void volume fraction is assumed at the grain boundary and inside grains. Since Gurson-like criteria have been noticed to account for periodic arrays of voids as well as random distributions without additional calibration (Hure, 2021), Eq. 18 is used to describe intergranular void growth and the following yield function (Paux et al., 2015) is chosen to account for transgranular void growth:

$$\lim_{m\to\infty}\left[\sum_{s=1}^{K}\left(\frac{\left|\mathbf{\Sigma}:\boldsymbol{\mu}_s\right|}{\tau_s^c}\right)^m\right]^{2/m} + 2qf\cosh\left(\kappa'\frac{\Sigma_m}{\tau^c}\right) - 1 - (qf)^2 = 0 \tag{43}$$

with $\kappa' = 0.489$ and $q$ given by Table 3. Since yield functions only differ due to the deviatoric term, $f$ and $T$ have no influence on which of the grain boundary or grain interiors will experience plasticity first. In fact, it was proven in Appendix C that at constant porosity and loading state, the porous boundary (modeled by Eq. 18) will always be harder than at least one of the two grain interiors (modeled by Eq. 43). Hence plasticity will first occur inside grains.

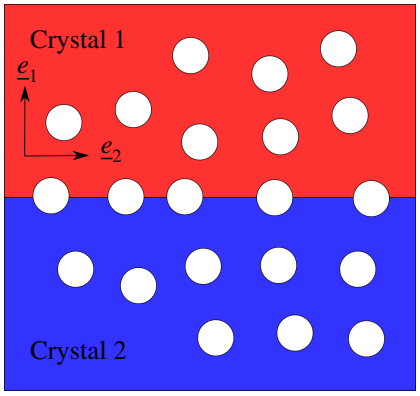


Figure 12: Porous bi-crystal with a random distribution of spherical cavities.

This general prediction is in agreement with the experimental evidence that transgranular fracture is more common than intergranular ductile fracture, the latter being triggered by specific weakening of grain boundaries.

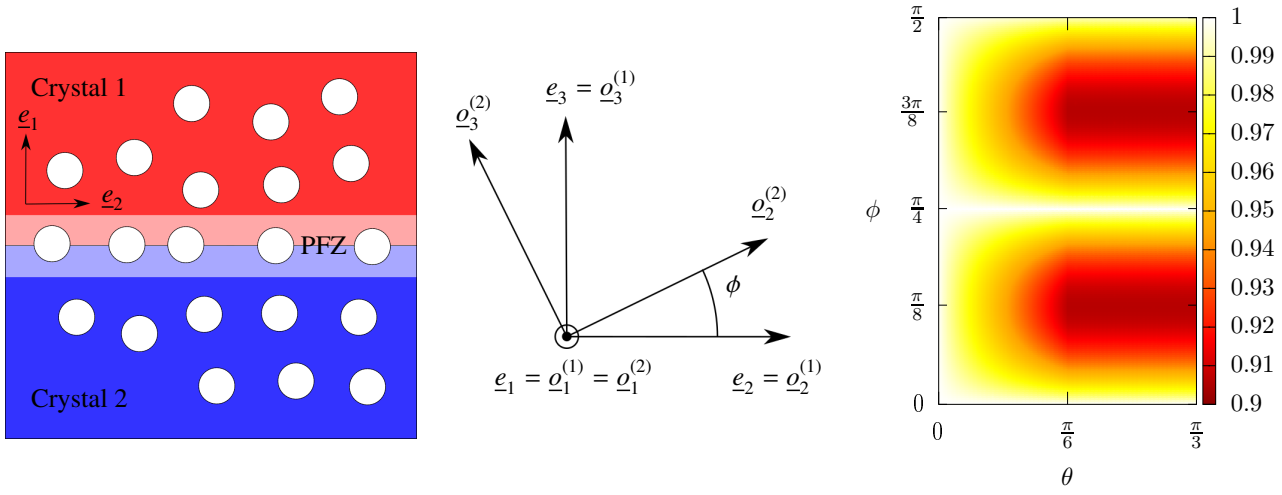


(a) (b) (c)

Figure 13: Effect of crystal orientation and Lode angle $\theta$ on void growth inside a porous rate-independent bi-crystal with a soft precipitate-free zone (PFZ): (a) microstructure considered; (b) orientation mismatch $\phi$ between crystal 1 of orthotropy axes ($\underline{o}_i^{(1)}$) and crystal 2 of orthotropy axes ($\underline{o}_i^{(2)}$); (c) threshold $\tau^c_{GB}/\tau^c_{GI}$ below which plasticity occur first at grain boundaries as a function of $\phi$ and $\theta$, at $T = 1/3$ and $f = 0.01$.

One of these weaknesses is the existence of a precipitate-free zone (PFZ) around grain boundaries of many precipitation-hardened alloys (see Fig. 13a), which results in a significant decrease of the mean critical shear stress at grain boundaries. This critical shear stress is denoted $\tau^c_{GB}$ (Eq. 18 is used with $\tau_s^{(1),c} = \tau_s^{(1),c} = \tau^c = \tau^c_{GB}$) while the grain interior critical shear stress is $\tau^c_{GI}$ (Eq. 43 is used with $\tau^c_s = \tau^c = \tau^c_{GI}$). Restricting the analysis to a particular case of bi-crystals whose first crystal has orthotropy axes aligned with the frame of reference and whose second crystal has been rotated by an angle $\phi$ around $\underline{e}_1$ (see Fig. 13b) — note that $\phi$ and $\phi + \pi/2$ result in the same crystal — , Fig. 13c shows the critical shear stress mismatch required to trigger void growth at grain boundaries at $T = 1/3$ (simple tension) and $f = 0.01$. The axial symmetry in $\phi$ relatively to $\phi = \pi/4$ was expected because exchanging crystal 1 with crystal 2 do not influence the result. Remark that for $\phi \in \{0, \pi/2\}$ or $\theta = 0$, the two crystals are indistinguishable so yielding will occur both at the grain boundary and at grain interiors at $\tau^c_{GB} = \tau^c_{GI}$; decreasing $\tau^c_{GB}$ under this threshold will localize plasticity at grain boundaries. In all other situations, crystals have different behaviors under the prescribed loading so the threshold $\tau^c_{GB}/\tau^c_{GI}$ displayed on Fig. 13c will be below 1. Lode angle $\theta$ and crystal orientation mismatch $\phi$ have an influence on the threshold – although no influence of $\theta$ is reported when it exceeds a value of $\pi/6$. Identical trends exist for other stress triaxiality ratios $T$ and void volume fractions $f$ — even if these results need to be interpreted carefully due to the potential occurrence of void coalescence at high $T$ and $f$. This is coherent with experimental results which show that some grain boundaries are more prone to intergranular fracture than others and provide a rationale to the existence of fracture surface exhibiting both transgranular and intergranular fracture (Deshpande et al., 1998). Note that inhomogeneities in the microstructure (Pommier et al., 2016) and grain boundary tilt angle relative the loading (Gräf and Hornbogen, 1977) have also been put forward to justify such findings. Since PFZ usually have a higher work-hardening rate than grain interiors, occurrence of plasticity at grain boundaries can be followed by grain interior plasticity once the PFZ has hardened (Thomas and Nutting, 1959). Therefore, the threshold given is an upper bound for the occurrence of ductile grain boundary failure, since $\tau^c_{GB}$ may be required to be much lower to account for subsequent fostered work-hardening; a full analysis of this effect was conducted by Pardoen et al. (2003) using isotropic GTN models.

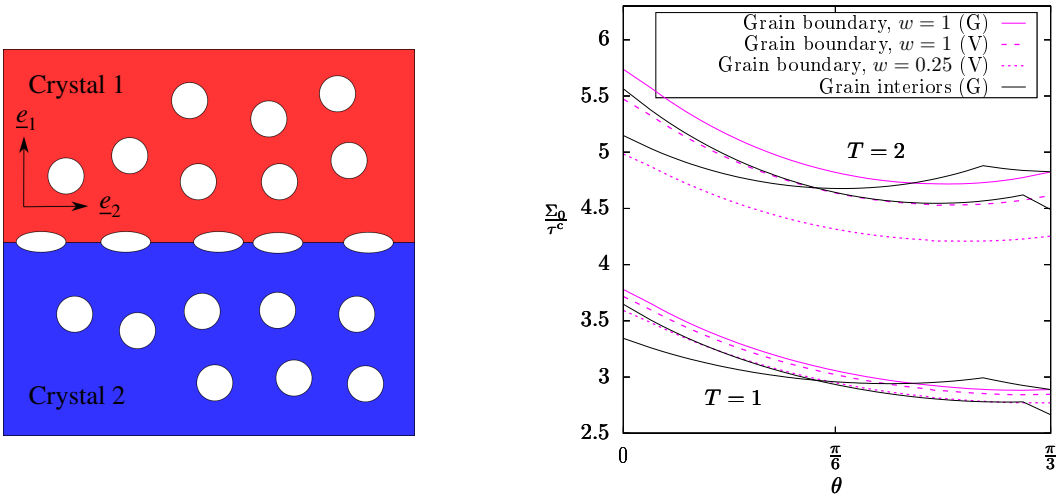


(a) (b)

Figure 14: Effect of intergranular void aspect ratio $w$, triaxiality $T$ and Lode angle $\theta$ on void growth inside a porous rate-independent polycrystal of fixed orientation couple #10: (a) microstructure considered; (b) normalized yield stress $\Sigma_0/\tau^c$ at grain interiors and at the grain boundary as a function of $\theta$ for various $w$ and $T$, computed either with Eq. 18 (G) or Eq. 36 (V).

Another weakness of grain boundaries that could enhance the occurrence of intergranular ductile fracture at constant void volume fraction is a different void aspect ratio. Indeed, elongated precipitates are common at grain boundaries (Kawabata and Izumi, 1976) and may lead to oblate intergranular voids. Thus, as a second example, microstructure shown in Fig. 14a is considered, with spheroidal cavities of void aspect ratio $w = w_2 = w_3$ at the grain interface (see Section 4.1 for the definition of these parameters), their volume being equal to the one of spherical voids located at grain interiors. The same crystal orientation couple as Fig. 11b is chosen. Normalized yield stresses of grain interiors as well as the grain boundary are plotted in Fig. 14b for $w = 1$ and $w = 0.25$ at two different triaxialities. Porous single crystals are still modeled with Eq. 43 but Gurson-like and variational criteria (Eqs. 18 and 36) are plotted for the porous boundary with $w = 1$; they are very close at $T = 1$ but the discrepancy increase with triaxiality — note that the two criteria coincide at the deviatoric point, at least when $f \to 0$. Despite this small inconsistency, the dependence in Lode angle $\theta$ is identical for the two criteria. Note that the brutal change in the slope of grain interior yield stress is not surprising; as pointed in Paux et al. (2018), it is related to a different set of slip systems being activated; no such vertexes are observed on grain boundary yield stress curves but no general rule can be stated on their absence as Eq. 43 is a special case of Eq. 18. As seen in Fig. 14b, transgranular yielding is favored at $T = 1$ for both $w = 1$ and $w = 0.25$, despite the expected softening effect of void aspect ratio reduction (see Fig. 11b). At $T = 2$ and $w = 1$, the same conclusion holds when using Eq. 18, as already pointed out in the previous case study. Due to the discrepancy between void growth criteria, this conclusion is challenged for $\theta > \pi/6$ when using the variational criterion, which underlines the paramount importance of quantitative prediction of yield stresses as small errors can influence the failure mode. Finally, since void shape softening increases with $T$, it is no surprise that intergranular yielding is favored over transgranular yielding at $T = 2$ and $w = 0.25$.

## 6. Conclusion and perspectives

Large-scale simulation of intergranular ductile fracture requires the development of yield criteria for porous grain boundaries. This study focused on the void growth stage, *i.e.* the regime in which plastic deformation is not yet localized at void scale. Using analytical homogenization techniques, two void growth yield criteria were derived for porous bi-crystal unit-cells. The first yield locus (Eq. 18), suited for rate-independent crystals with spherical voids, was obtained through limit-analysis of Hill plastic materials followed by heuristical corrections of the deviatoric and hydrostatic terms. This criterion is a Gurson-like expression, meaning that it can be easily implemented in mechanical solvers (FEM or FFT) that already hold similar models. Following a variational approach, an alternative criterion was derived for viscoplastic crystals of Norton exponent $n$: Hashin-Strikman estimates are obtained rigorously for $n = 1$ (Eqs. 23, 29), and a heuristical extension to $n > 1$ is proposed (Eq. 36). Using a database of small strain unit-cell computations of porous grain boundaries, the agreement of models with respect to simulations was checked. Both criteria make satisfying predictions of yield surfaces for arbitrary macroscopic stress tensors (Fig. 6c,d; Figs. 8-11c,d) and crystal orientation couples (Fig. 6a,b, Figs. 8-11a). The span of porosities in which the models are validated is quite large ($f \in [0.001, 0.3]$), and the variational criterion predicts correctly gauge surfaces for ellipsoidal voids shapes whose axes are aligned with unit-cell axes (Figs. 8-11b), which exclude the modeling of void rotation effects.

The derivation of intergranular void growth criteria, as performed in this paper, is an important milestone to simulate grain boundary ductile fracture. To describe the full yield/gauge surfaces of voided grain boundaries, a void coalescence criterion should also be obtained, as performed in Hure (2019) for voided single crystals. Once the multi-surface criterion is complete, the addition of suitable evolution laws for microstructural parameters, such as porosity and void shape, will constitute a full homogenized model, as was collected in Sénac et al. (2022) for porous single crystals. Thus, microstructure-informed simulations of the competition between transgranular and intergranular ductile fracture could be

envisioned, as pioneered in Pardoen et al. (2003) for a given material, using isotropic models. Concomitantly, reference experiments are needed in order to assess theoretical models: namely, the hypothesis of perfect bonding between crystals made in crystal plasticity simulations and analytical homogenization have to be assessed. Such confrontations at the bi-crystal scale are scarce (*e.g.* Zaefferer et al. (2003)) and were never performed in presence of a voided boundary. Besides, if the material of interest display intergranular voids of radius lower than the plasticity characteristic length, extension of these criteria to account for size effects may be needed — see Khavasad and Keralavarma (2021) on that subject. Finally, at a different scale, it is of paramount importance to compare porous polycrystal fracture predictions with actual experiments in the case of small aggregates so that the homogenization of crystallographic effects is validated.

## CRediT authorship contribution statement

**Cédric Sénac:** Conceptualization, Methodology, Software, Validation, Formal analysis, Data curation, Writing - original draft, Writing - review & editing, Visualization. **Jérémy Hure:** Conceptualization, Methodology, Formal analysis, Writing - review & editing, Funding acquisition. **Benoît Tanguy:** Conceptualization, Writing - review & editing, Funding acquisition.

## Appendix A. Definition and properties of Hill strain anisotropy tensor $\mathbb{H}^*$

For every orthonormal basis $(\underline{e}_1, \underline{e}_2, \underline{e}_3)$, the following set of vectors is a basis of the space of deviatoric symmetric second-order tensors $\mathscr{D}_2(\mathbb{R})$ (*i.e.* symmetric tensors $\boldsymbol{A}$ such that $\mathbb{J} : \boldsymbol{A} = 0$):

$$\left( \frac{\sqrt{3}+1}{2} \underline{e}_2 \otimes \underline{e}_2 + \frac{\sqrt{3}-1}{2} \underline{e}_3 \otimes \underline{e}_3, \frac{\sqrt{3}-1}{2} \underline{e}_2 \otimes \underline{e}_2 + \frac{\sqrt{3}+1}{2} \underline{e}_3 \otimes \underline{e}_3, \sqrt{2}\underline{e}_2 \otimes \underline{e}_3, \sqrt{2}\underline{e}_3 \otimes \underline{e}_1, \sqrt{2}\underline{e}_1 \otimes \underline{e}_2 \right) \tag{A.1}$$

Since $\mathscr{D}_2(\mathbb{R})$ is stabilized by $\mathbb{H}_i$, it is legitimate to consider its restriction $\overline{\mathbb{H}}_i$ to that subspace. The hypothesis that matrix materials can accommodate arbitrary isochoric deformation is made, *i.e.* $\overline{\mathbb{H}}_i$ admits an inverse tensor $\overline{\mathbb{H}}_i^*$. Tensors $\overline{\mathbb{H}}_i^*$ are then extended over the full space of symmetric second-order tensors $\mathscr{S}_2(\mathbb{R}) = \mathscr{D}_2(\mathbb{R}) \oplus \mathbb{R}\boldsymbol{I}$ by prescribing their value to 0 over the second set of the direct sum, yielding Hill strain anisotropy tensors $\mathbb{H}_i^*$ that verify $\mathbb{H}^* : \mathbb{H} = \mathbb{H} : \mathbb{H}^* = \mathbb{K}$.

The Voigt-Mandel condensation of $\mathbb{H}^*$ associated with an orthonormal basis of orthotropy $(\underline{e}_\mathrm{I}, \underline{e}_\mathrm{II}, \underline{e}_\mathrm{III})$ writes:

$$\mathbb{H}^* = \begin{pmatrix} h_{11}^* & h_{12}^* & h_{31}^* & 0 & 0 & 0 \\ h_{12}^* & h_{22}^* & h_{23}^* & 0 & 0 & 0 \\ h_{31}^* & h_{23}^* & h_{33}^* & 0 & 0 & 0 \\ 0 & 0 & 0 & h_{44}^* & 0 & 0 \\ 0 & 0 & 0 & 0 & h_{55}^* & 0 \\ 0 & 0 & 0 & 0 & 0 & h_{66}^* \end{pmatrix} \tag{A.2}$$

and it can be checked that this matrix admits an arrangement $(h_i^*)_{i\in[\![1,6]\!]}$ of its eigenvalues verifying the following relations:

$$\begin{array}{lll} h_{11}^* = \frac{1}{9}\left(4h_1^* + h_2^* + h_3^*\right) & h_{23}^* = \frac{1}{9}\left(h_1^* - 2h_2^* - 2h_3^*\right) & h_{44}^* = h_4^* \\ h_{22}^* = \frac{1}{9}\left(h_1^* + 4h_2^* + h_3^*\right) & h_{31}^* = \frac{1}{9}\left(-2h_1^* + h_2^* - 2h_3^*\right) & h_{55}^* = h_5^* \\ h_{33}^* = \frac{1}{9}\left(h_1^* + h_2^* + 4h_3^*\right) & h_{12}^* = \frac{1}{9}\left(-2h_1^* - 2h_2^* + h_3^*\right) & h_{66}^* = h_6^* \end{array} \tag{A.3}$$

## Appendix B. Coalescence micromechanical indicator

The range of stress triaxialities and porosities covered in Section 2 makes it likely that some unit-cells undergo void coalescence instead of void growth. Therefore, an indicator is needed to filter out simulations that display deformation modes that are outside the scope of this study. Two main macroscopic coalescence indicators have been proposed. First, coalescence by internal necking can be indicated by vanishing transverse strain rates $D_{22}, D_{33}$ compared to $D_{11}$. However, this indicator cannot account for coalescence outside the $(\underline{e}_2, \underline{e}_3)$-plane such as shear-assisted coalescence (Hure, 2019) or coalescence in columns (Gologanu et al., 2001). The extension proposed by Cadet et al. (2021) is based on the decrease rate of $\det(\dot{\boldsymbol{F}})$ — where $\boldsymbol{F}$ is the deformation gradient at the scale of the unit-cell — which experiences a drastic change when plasticity localizes. Unfortunately, in small strain simulations, unit-cells are not expected to experience successive void growth and coalescence but rather a unique deformation mode, making this extension unsuitable. Second, Rice criterion for plastic localization (Rice, 1976) is an alternative way of detecting the onset of coalescence, as discussed in Vishwakarma and Keralavarma (2019) and Cadet et al. (2022). However, the start of inhomogeneous yielding under shear-dominated loadings is not detected by this criterion (Torki et al., 2021) and the fourth-order elasto-plastic tangent stiffness tensor is not computed during FFT mechanical solving and thus cannot be obtained from unit-cell simulations.

In order to break this stalemate, advantage is taken from microscopic slip activity $\dot{\Gamma} = \sum_s |\dot{\gamma}_s|$ fields that are available upon plastic yielding for all simulations (Fig. B.15a,c). Statistical analysis of $\dot{\Gamma}$ values in voxels belonging to crystalline phases unveils different distributions according to the activated deformation mode, as shown in Fig. B.15b,d. In void growth situations (Fig. B.15a,b), plasticity is homogeneous around mean slip activity $\left\langle \dot{\Gamma} \right\rangle$ with very few voxels experiencing no yielding; this is in agreement with classical terminology of "diffuse plasticity". On the contrary, void coalescence

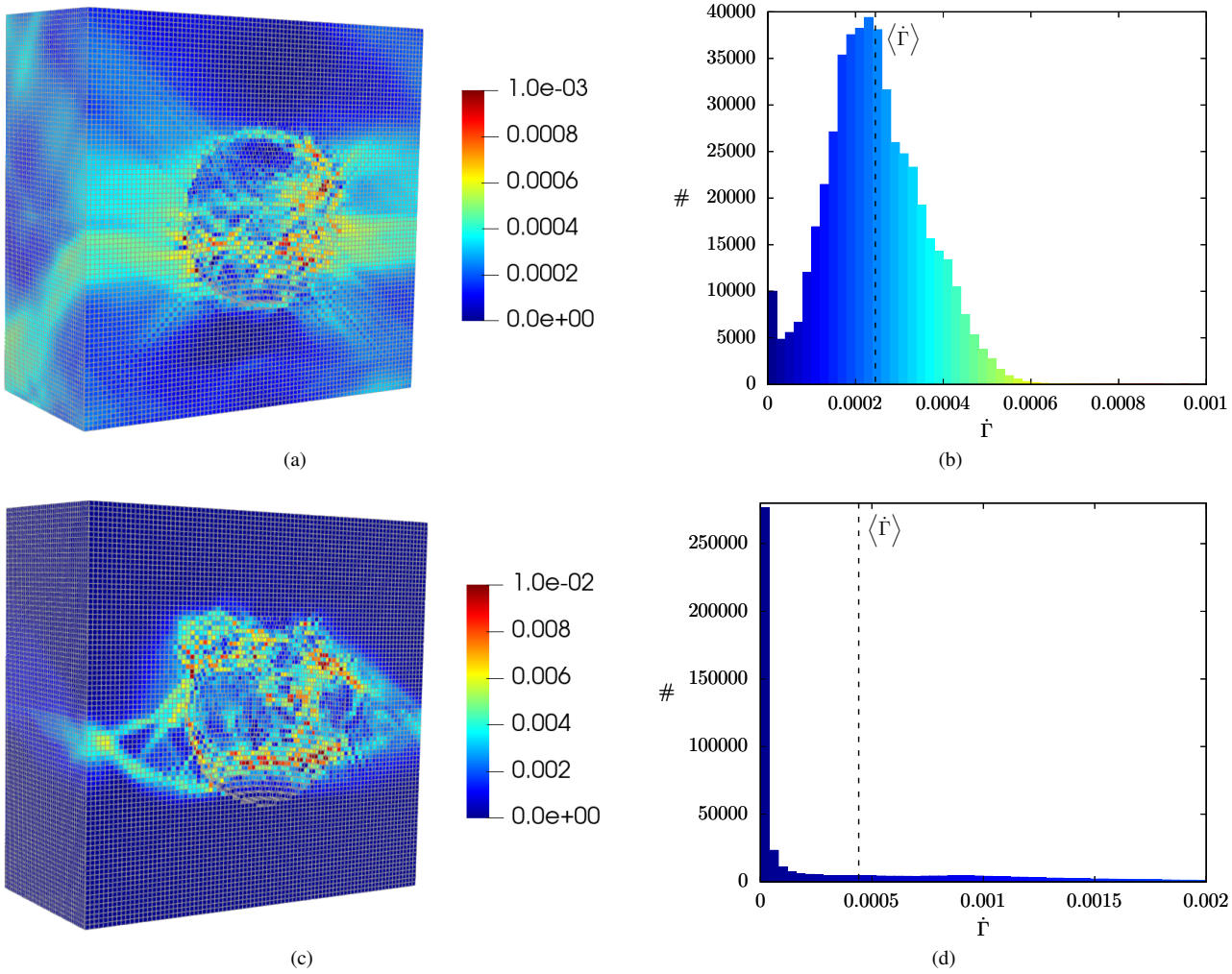


Figure B.15: Microscopic field (a,c) and corresponding histograms (c,d) of $\dot{\Gamma}$ at macroscopic plastic yielding for orientation couple #9, $\theta = 0$, $n = 100$ and $f = 0.05$: (a,b) $T = 0$; (b,c) $T = 10$.

is associated with large elastic zones in the unit-cell (Fig. B.15c,d), leading to a distribution strongly weighted around 0 while mean slip activity $\langle\dot{\Gamma}\rangle$ is driven by voxels located in ligaments where plasticity localizes. Between these two well-identified extremes, few simulations remain ambiguous.

Based on the previous findings, the following coalescence indicator is proposed:

$$\Xi \geq \delta \quad \text{where} \quad \Xi = \frac{\langle\dot{\Gamma}\rangle}{\text{median}\left(\dot{\Gamma}\right)} \in [0, +\infty] \tag{B.1}$$

$\Xi$ indicates the level of localization in the matrix and $\delta$ is an adjustable threshold. If $\Xi \geq \delta$, it means that the strain rate field deviates too much from a normal distribution, *i.e.* plasticity is no longer diffuse. For this study, a careful examination of the database ensured that the choice of $\delta = 1.5$ was satisfying for $n = 100$ and $\delta = 1.35$ for lower $n$. On Fig. B.16 are shown a few interesting properties of this indicator. First, $\Xi$ is an increasing function of $T$ from low to high triaxialities – as expected given the transition from growth to coalescence – but often exhibits a drop at very high triaxialities due to the transition from internal necking coalescence to multi-directional coalescence, a deformation mode in which localization takes place in a greater proportion of the unit-cell (this issue was briefly mentioned in Keralavarma (2017) and Keralavarma et al. (2020)). Second, when porosity increases, coalescence takes place at lower triaxialities. Finally, mesh discretization $N$ has only a marginal effect on $\Xi$: indeed, in porous unit-cells, strain localization is mainly controlled by the cavity size and not much by mesh refinement. Note that Chouksey et al. (2019) did propose another micromechanical indicator, but with less marked trends.

## Appendix C. Crystalline laminate mechanical analysis

Considering a unit-cell containing a crystalline laminate subjected to periodic boundary conditions, Hill-Mandel lemma $\boldsymbol{\Sigma} : \boldsymbol{D} = \langle\boldsymbol{\sigma} : \boldsymbol{d}\rangle_\Omega$ is verified with macroscopic stress $\boldsymbol{\Sigma}$ being the volume-average of the deviatoric microscopic field: $\boldsymbol{\Sigma} = \langle\boldsymbol{\sigma}\rangle_\Omega = \frac{1}{2}\left(\langle\boldsymbol{\sigma}\rangle_{\Omega_1} + \langle\boldsymbol{\sigma}\rangle_{\Omega_2}\right)$. Stress fields $\boldsymbol{\sigma}$ that are constant in each crystal are statistically admissible as long as $\boldsymbol{\sigma}^{(1)} = \boldsymbol{\Sigma} + \boldsymbol{\Delta}_n$ and $\boldsymbol{\sigma}^{(2)} = \boldsymbol{\Sigma} - \boldsymbol{\Delta}_n$ with $\boldsymbol{\Delta}_n$ an element of the space $\mathscr{C}_2(\mathbb{R})$ of symmetric second-order tensors satisfying

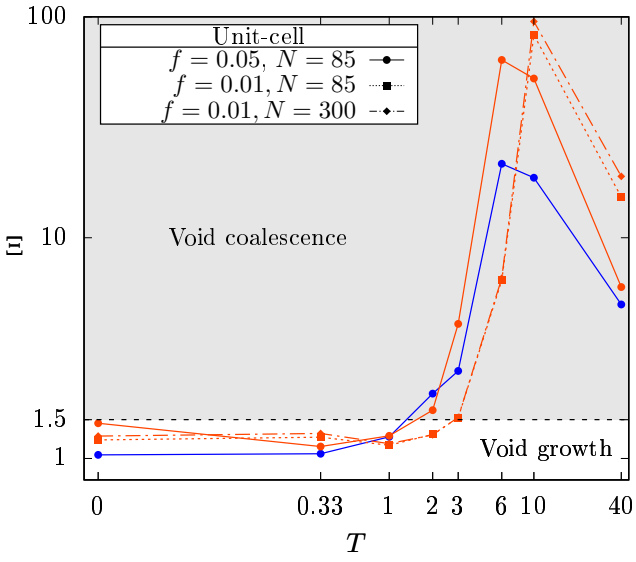


Figure B.16: Coalescence indicator $\Xi$ as a function of triaxiality $T$ at $\theta = 0$ and $n = 100$ for various porosities, mesh discretizations and crystal orientations.

the stress continuity condition at the planar interface. Then, every statically admissible field $\boldsymbol{\sigma}$ is such that:

$$\langle u(\boldsymbol{\sigma})\rangle_\Omega = \frac{1}{2}\left[\left\langle u_n^{(1)}(\boldsymbol{\sigma})\right\rangle_{\Omega_1} + \left\langle u_n^{(2)}(\boldsymbol{\sigma})\right\rangle_{\Omega_2}\right] \geq \frac{1}{2}\left[u_n^{(1)}\left(\langle\boldsymbol{\sigma}\rangle_{\Omega_1}\right) + u_n^{(2)}\left(\langle\boldsymbol{\sigma}\rangle_{\Omega_2}\right)\right] = \frac{1}{2}\left[u_n^{(1)}(\boldsymbol{\Sigma}+\boldsymbol{\Lambda}_n) + u_n^{(2)}(\boldsymbol{\Sigma}-\boldsymbol{\Lambda}_n)\right] \tag{C.1}$$

due to the convexity of $u_n^{(1)}$ and $u_n^{(2)}$ in $\boldsymbol{\sigma}$ (potentials $u$ are defined and discussed at the beginning of Section 4). Therefore, minimizing the macroscopic stress potential over statically admissible stress fields (Eq. 21) amounts to a minimization over crystal-wise constant fields, *i.e.* finding $\boldsymbol{\Lambda}_n = \widetilde{\boldsymbol{\Lambda}_n}$ so that $U$ is minimal:

$$U(\boldsymbol{\Sigma}) = \min_{\boldsymbol{\Lambda}_n \in \mathscr{C}_2(\mathbb{R})} \frac{1}{2}\left[u_n^{(1)}(\boldsymbol{\Sigma}+\boldsymbol{\Lambda}_n) + u_n^{(2)}(\boldsymbol{\Sigma}-\boldsymbol{\Lambda}_n)\right] \tag{C.2}$$

In the rate-independent limit, $n \to +\infty$ so Eq. 17 is obtained. From Eq. C.2, it can be easily shown that the potential of the bi-crystal is lower than at least one of the corresponding single crystals: $U(\boldsymbol{\Sigma}) \leq U(\boldsymbol{\Sigma}, \boldsymbol{\Lambda}_n = 0) \leq \max(U_1(\boldsymbol{\Sigma}), U_2(\boldsymbol{\Sigma}))$ which proves that in the limit $f \to 0$, the porous bi-crystal will always be less prone to yielding at deviatoric loadings than one of the constitutive single crystals (see Section 2.3). Note that when crystal 1 and crystal 2 are equal, $u_n^{(1)} = u_n^{(2)} = u_n$ and using the convexity of $u_n$ on Eq. C.1 yield $U(\boldsymbol{\Sigma}) = u_n(\boldsymbol{\sigma})$, *i.e.* the unnecessary stress continuity equation vanishes through the choice $\widetilde{\boldsymbol{\Lambda}_n} = 0$.

For $n = 1$, an explicit resolution can be conducted. Indeed, Eq. C.2 can be rewritten using tensor $\mathbb{E}$ enforcing continuity at the planar interface (Hill, 1972), which enables to perform the minimization over the space of symmetric tensors:

$$U(\boldsymbol{\Sigma}) = \min_{\boldsymbol{\Lambda} \in \mathscr{S}_2(\mathbb{R})} \frac{\dot{\gamma}_0 \tau^c}{4}\left[(\boldsymbol{\Sigma}+\mathbb{E}:\boldsymbol{\Lambda}):\mathbb{S}_1:(\boldsymbol{\Sigma}+\mathbb{E}:\boldsymbol{\Lambda}) + (\boldsymbol{\Sigma}-\mathbb{E}:\boldsymbol{\Lambda}):\mathbb{S}_2:(\boldsymbol{\Sigma}-\mathbb{E}:\boldsymbol{\Lambda})\right] \tag{C.3}$$

$\boldsymbol{\Lambda}$-derivation and an inversion in the subspace of fourth order tensors invariable by left or right double contraction with $\mathbb{E}$ (whose multiplicative identity is $\mathbb{E}:\mathbb{I}:\mathbb{E}$) yield:

$$\begin{aligned} \widetilde{\boldsymbol{\Lambda}_1} &= \mathbb{D}:\boldsymbol{\Sigma} \quad \text{with} \quad \mathbb{D} = \mathbb{E}:\left[\mathbb{E}:(\mathbb{S}_1+\mathbb{S}_2):\mathbb{E}\right]^{-1}:\left[\mathbb{E}:(\mathbb{S}_2-\mathbb{S}_1)\right] \\ U(\boldsymbol{\Sigma}) &= \frac{\dot{\gamma}_0\tau^c}{2}\boldsymbol{\Sigma}:\overline{\mathbb{S}}:\boldsymbol{\Sigma} \quad \text{with} \quad \overline{\mathbb{S}} = \frac{1}{2}\mathbb{K}:\left[(\mathbb{I}+\mathbb{D}):\mathbb{S}_1:(\mathbb{I}+\mathbb{D}) + (\mathbb{I}-\mathbb{D}):\mathbb{S}_2:(\mathbb{I}-\mathbb{D})\right]:\mathbb{K} \end{aligned} \tag{C.4}$$

However, when $n > 1$, minimization amounts to finding the roots of high degree polynomials of three variables, which seems to forbid explicit resolution. Thus, it must be resorted to numerical optimization to find $\widetilde{\boldsymbol{\Lambda}_n}$. Nelder-Mead algorithm (Nelder and Mead, 1965) with multiple random starting points was found to be an efficient method to conduct this minimization.

Note that the constant character of microscopic stress fields in crystals is not retained when a cavity is present or when grain boundaries are not planar; indeed, stress continuity conditions at these interfaces applied to constant stress fields yield $\boldsymbol{\sigma} = 0$.

## Appendix D. Analytic expressions of $g$-functions

In this section are provided expressions of $g_0$ and $g_1$ for both ellipsoidal and elliptic-cylindrical voids with one axis along $\underline{e}_1$. $g_2$ is obtained immediately from $g_1$ by noticing that $g_2\left(\underline{\xi}\right) = g_1\left(-\underline{\xi}\right)$. The following notations, where $\odot$ is the Hadamard product, are introduced:

$$\phi = \left\|\underline{\xi}\odot r_1\underline{e}_1\right\|_2 \;,\; \zeta = \left\|\underline{\xi}\odot\left(r_2\underline{e}_2 + r_3\underline{e}_3\right)\right\|_2 \;,\; \eta = \left\|\underline{\xi}\odot\left(r_1\underline{e}_1 + r_2\underline{e}_2 + r_3\underline{e}_3\right)\right\|_2 \tag{D.1}$$

Voids without an axis along $\underline{e}_1$ do not follow the formulas given below and use must be made of the general expression Eq. 26.

*Appendix D.1. Ellipsoidal voids*

The unit-cell configuration corresponding to ellipsoidal cavities is shown on Fig. D.17. After a variable substitution and the choice of the spherical coordinates of main axis along $\underline{\xi}$, $g_0$ can be expressed as:

$$g_0\left(\underline{\xi}\right) = \frac{3}{4\pi}\int_{r=0}^{1}\left(\int_{\theta=0}^{\pi}\left(\int_{\phi=0}^{2\pi} e^{i\eta r\cos\theta} r^2\sin\theta\,\mathrm{d}\phi\right)\mathrm{d}\theta\right)\mathrm{d}r = 3\,\frac{\sin\eta-\eta\cos\eta}{\eta^3} \tag{D.2}$$

$g_1$, on its part, require the computation of the Fourier transform of the characteristic function of a cube and of a demi-ball:

$$g_1\left(\underline{\xi}\right) = \frac{2}{1-f}\left[\frac{i}{n_1\pi}\sin\!\left(\frac{n_1\pi}{2}\right)^2\delta_{n_2,0}\delta_{n_3,0} - \int_{\underline{x}\in\Omega_0^+} e^{i\underline{\xi}\cdot\underline{x}}\right] \tag{D.3}$$

with $\Omega_0^+ = \left\{\underline{x}\in\Omega_0\,,\ \underline{x}\cdot\underline{e}_1 > 0\right\}$. Unfortunately, to the knowing of the authors, the latter do not possess a closed-form, even if its real part is known. However, it can be expressed for $(n_2, n_3) \neq (0,0)$ as a one-dimensional integral (Eq. D.4$_b$) or as a series (Eq. D.4$_e$), the latter being numerically more efficient by two orders of magnitude:

$$\begin{aligned}
\int_{\underline{x}\in\Omega_0^+} e^{i\underline{\xi}\cdot\underline{x}} &= r_1r_2r_3\int_0^1\left(\int_0^{\sqrt{1-x_3^2}}\left(\int_0^{2\pi} e^{i\zeta r\cos\theta}e^{i\phi x_3} r\mathrm{d}\theta\right)\mathrm{d}r\right)\mathrm{d}x_3\\
&= \frac{3f}{2\zeta}\int_0^1 e^{i\phi x_3}\sqrt{1-x_3^2}\,J_1\left(\zeta\sqrt{1-x_3^2}\right)\mathrm{d}x_3\\
&= \frac{f}{2}\left[g_0\left(\underline{\xi}\right) + \frac{3}{\zeta}\,\mathrm{Im}\left(\int_0^1 e^{i\phi\sqrt{1-t^2}}\,\frac{t^2}{\sqrt{1-t^2}}J_1(\zeta t)\mathrm{d}t\right)\right]\\
&= \frac{f}{2}\left[g_0\left(\underline{\xi}\right) + i\frac{3}{\zeta}\sum_{n=0}^{+\infty}(-1)^n\frac{\phi^{2n+1}}{(2n+1)!}\int_0^1 t^2\left(1-t^2\right)^n J_1(\zeta t)\mathrm{d}t\right]\\
&= \frac{f}{2}\left[g_0\left(\underline{\xi}\right) + i\frac{3\phi}{\zeta^2}\sum_{n=0}^{+\infty}\left(-\frac{2\phi^2}{\zeta}\right)^n\frac{n!}{(2n+1)!}J_{n+2}(\zeta)\right]
\end{aligned} \tag{D.4}$$

where $J_n$ is the $n^{\text{th}}$ Bessel function. For $(n_2, n_3) = 0$, the following value is obtained:

$$\int_{\underline{x}\in\Omega_0^+} e^{i\underline{\xi}\cdot\underline{x}} = \frac{f}{2}\left[g_0\left(\underline{\xi}\right) + i\frac{3}{\phi^3}\left(1-\cos\phi-\phi\sin\phi+\frac{1}{2}\phi^2\right)\right] \tag{D.5}$$

*Appendix D.2. Elliptic-cylindrical voids*

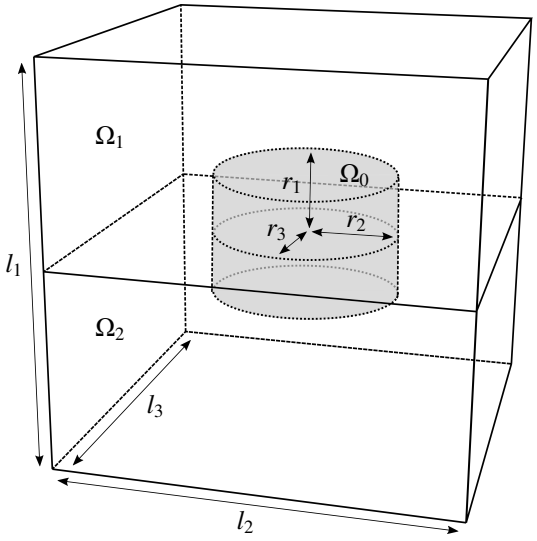


Figure D.17: Rectangular prismatic unit-cell with centered elliptic-cylindrical cavity; void axes are aligned with unit-cell axes.

Given the additional computation time brought by $g_1$ evaluation for ellipsoidal cavities, it may be more convenient to consider a laminate with elliptic cylindrical voids, shown in Fig. D.17. In that case, $g$-functions are Fourier transforms of characteristic functions of elliptic cylinders (or complementary of those for $g_1$ and $g_2$) and formulas are found below:

$$\begin{aligned}
g_0\left(\underline{\xi}\right) &= 2\,\frac{\sin(\phi)}{\phi}\,\frac{J_1(\zeta)}{\zeta}\\
g_1\left(\underline{\xi}\right) &= \frac{2}{1-f}\left[\frac{i}{n_1\pi}\sin\!\left(\frac{n_1\pi}{2}\right)^2\delta_{n_2,0}\delta_{n_3,0} - 2f\,\frac{\sin\left(\frac{\phi}{2}\right)}{\phi}\,\frac{J_1(\zeta)}{\zeta}e^{i\frac{\phi}{2}}\right]
\end{aligned} \tag{D.6}$$

keeping in mind that $\frac{J_1(\zeta)}{\zeta} \longrightarrow \frac{1}{2}$ when $\zeta \to 0$. All equations given in Sections 4.1 and 4.3 in the context of ellipsoidal voids are still valid for elliptic-cylindrical voids, except Eq. 41 in which $a = \sqrt{3}$ for circular-cylindrical voids.

Given an ellipsoidal void of demi-axes $(r_1, r_2, r_3)$, an equivalent elliptic-cylindrical void with dimensions $(r_1, r_2, \hat{r}_3)$ can be defined, with similar section in the plane $(\underline{e}_2, \underline{e}_3)$ and $\hat{r}_3$ chosen so that porosity $f$ is kept constant between the two unit-cells. Comparisons of gauge surfaces of spherical cavities and equivalent cylindrical cavities are shown in Fig. D.18 for $n = 1$ and $n = 100$ at fixed Lode angle $\theta = 0$. At $n = 1$, the reversibility domain increases when the void shape is changed from spherical to cylindrical; this property is not retained at $n = 100$ due to different values of $a$ in the heuristic extension. Regardless of $n$, a good agreement is reported when $f < 0.01$ for stress triaxialities ratios ranging from low to moderate — *i.e.* the part where void growth is active. However, this assessment should be pursued with other void shapes and more diverse loadings.

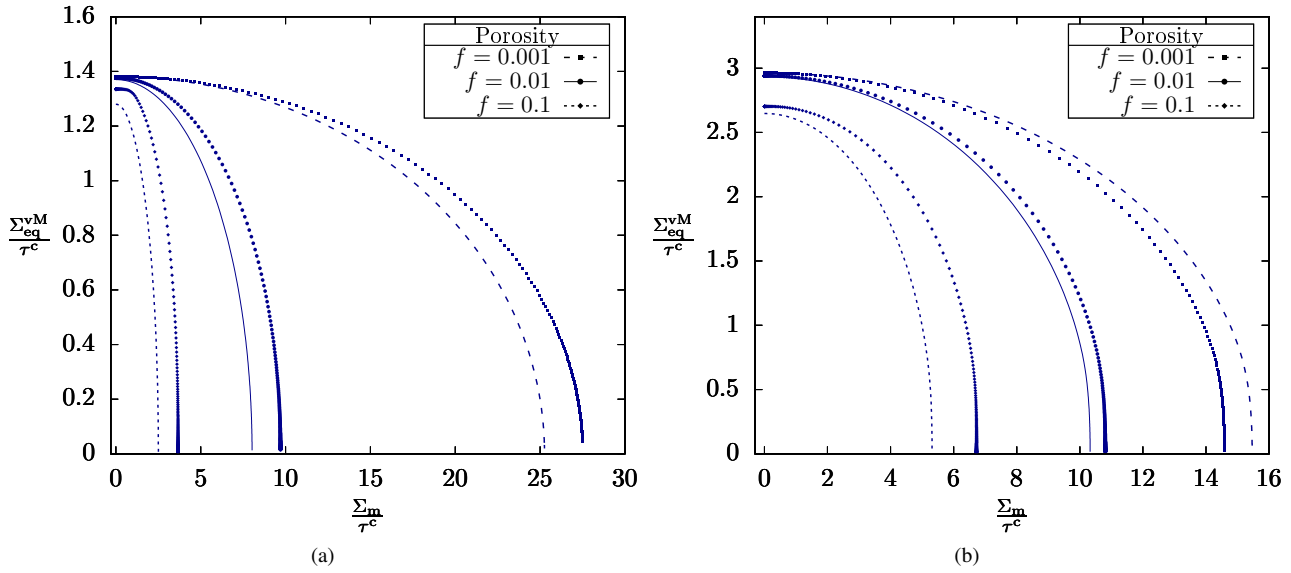


Figure D.18: Comparison of gauge surfaces predicted by variational estimates for spherical voids (lines) and equivalent cylindrical voids (points) at $\theta = 0$: (a) $n = 1$; (b) $n = 100$.

## Appendix E. Porous crystal with infinite equivalent equiangular slip systems

### *Appendix E.1. Pristine crystal*

In the principal frame $(\underline{e}_I, \underline{e}_{II}, \underline{e}_{III})$ of the Cauchy stress $\boldsymbol{\sigma}$, the following relation is verified:

$$\boldsymbol{\sigma} = \sigma_{\mathrm{m}} \boldsymbol{I} + \frac{2}{3} \sigma^{\mathrm{vM}}_{\mathrm{eq}} \boldsymbol{\sigma}^{(0)} \quad \text{with} \quad \boldsymbol{\sigma}^{(0)} = \begin{pmatrix} \cos\theta & 0 & 0 \\ 0 & -\cos\left(\theta + \frac{\pi}{3}\right) & 0 \\ 0 & 0 & -\cos\left(\theta - \frac{\pi}{3}\right) \end{pmatrix} \tag{E.1}$$

which means that when slip systems are equivalent, the plastic potential (Eq. 19) writes as:

$$u_n(\boldsymbol{\sigma}) = \frac{\dot{\gamma}_0 \, (\tau^{\mathrm{c}})^{-n}}{n+1} \left( \frac{2}{3} \sigma^{\mathrm{vM}}_{\mathrm{eq}} \right)^{n+1} \sum_{s=1}^{K} \left| \boldsymbol{\mu}_s : \boldsymbol{\sigma}^{(0)} \right|^{n+1} \tag{E.2}$$

In the limit of $K$ equiangular slip systems with $K \to +\infty$, the Riemann summation theorem yields:

$$\frac{1}{K} \sum_{s=1}^{K} \left| \boldsymbol{\mu}_s : \boldsymbol{\sigma}^{(0)} \right|^{n+1} \longrightarrow \left\langle \left| \boldsymbol{\mu} : \boldsymbol{\sigma}^{(0)}(\theta) \right|^{n+1} \right\rangle_{\mathcal{S}} \tag{E.3}$$

where $\mathcal{S}$ is the set of all possible slip systems. Any slip system can be obtained by rotating an arbitrary slip system, *e.g.* $\underline{s}_0 = \underline{e}_I$, $\underline{m}_0 = \underline{e}_{II}$ and $\boldsymbol{\mu}_0 = \mathrm{sym}\left[\underline{e}_I \otimes \underline{e}_{II}\right]$. Therefore, the right-hand side of Eq. E.3 can be calculated by performing the following integration over the set $SO_3(\mathbb{R})$ of three-dimensional rotations with the (uniform and unit-normalized) Haar measure $\lambda$ (Naimark, 1964):

$$\left\langle \left| \boldsymbol{\mu} : \boldsymbol{\sigma}^{(0)}(\theta) \right|^{n+1} \right\rangle_{\mathcal{S}} = \int_{SO_3(\mathbb{R})} \left| (\boldsymbol{R}^{\mathsf{T}} \cdot \boldsymbol{\mu}_0 \cdot \boldsymbol{R}) : \boldsymbol{\sigma}^{(0)} \right|^{n+1} \mathrm{d}\lambda(\boldsymbol{R}) \tag{E.4}$$

Recalling that $SO_3(\mathbb{R})$ can be parametrized with Euler angles $(\alpha_1, \alpha_2, \alpha_3) \in [0, 2\pi] \times [0, \pi] \times [0, 2\pi]$ with

$$\boldsymbol{R}(\alpha_1, \alpha_2, \alpha_3) = \begin{pmatrix} \cos\alpha_1 & -\sin\alpha_1 & 0 \\ \sin\alpha_1 & \cos\alpha_1 & 0 \\ 0 & 0 & 1 \end{pmatrix} \cdot \begin{pmatrix} 1 & 0 & 0 \\ 0 & \cos\alpha_3 & -\sin\alpha_3 \\ 0 & \sin\alpha_3 & \cos\alpha_3 \end{pmatrix} \cdot \begin{pmatrix} \cos\alpha_3 & -\sin\alpha_3 & 0 \\ \sin\alpha_3 & \cos\alpha_3 & 0 \\ 0 & 0 & 1 \end{pmatrix} \tag{E.5}$$

in the frame $(\underline{e}_I, \underline{e}_{II}, \underline{e}_{III})$, the integral can be recast as:

$$\left\langle \left| \boldsymbol{\mu} : \boldsymbol{\sigma}^{(0)}(\theta) \right|^{n+1} \right\rangle_{\mathcal{S}} = \frac{1}{8\pi^2} \int_0^{2\pi} \int_0^{\pi} \int_0^{2\pi} \left| [\boldsymbol{R}(\alpha_1, \alpha_2, \alpha_3)^{\intercal} \cdot \boldsymbol{\mu}_0 \cdot \boldsymbol{R}(\alpha_1, \alpha_2, \alpha_3)] : \boldsymbol{\sigma}^{(0)} \right|^{n+1} \sin\alpha_2 \, \mathrm{d}\alpha_3 \mathrm{d}\alpha_2 \mathrm{d}\alpha_1 \tag{E.6}$$

Restricting the analysis to odd $n$, a general form for this integral can be obtained using a formal computation tool:

$$\left\langle \left| \boldsymbol{\mu} : \boldsymbol{\sigma}^{(0)}(\theta) \right|^{n+1} \right\rangle_{\mathcal{S}} = a_n - \sum_{k=1}^{\lfloor \frac{n+1}{6} \rfloor} b_{k,n} \cos(6k\theta) \quad \text{with} \quad a_n, \, b_{k,n} > 0 \tag{E.7}$$

For instance:

$$a_1 = \frac{3}{20} \; ; \quad a_3 = \frac{27}{560} \; ; \quad a_5 = \frac{1269}{64064} \; , \quad b_{1,5} = \frac{27}{32032} \; ; \quad a_7 = \frac{5751}{622336} \; , \quad b_{1,7} = \frac{81}{77792} \tag{E.8}$$

In the limit $K \to +\infty$, the sum over $k$ in Eq. E.2 will contain an infinity of terms. In order for the potential $u_n$ to remain finite, $\tau^c$ must decrease with $K$ at a rate suggested by Eq. E.3. Therefore, the pristine single crystal is considered with renormalized CRSS $\tau^c = K^{1/n}\sigma^c$, so that:

$$u_n(\boldsymbol{\sigma}) \underset{K \to +\infty}{\longrightarrow} u_\infty(\boldsymbol{\sigma}) = \frac{\dot{\gamma}_0 \, (\sigma^c)^{-n}}{n+1} \left( g_n(\theta) \, \sigma_{\mathrm{eq}}^{\mathrm{vM}} \right)^{n+1} \quad \text{where} \quad g_n(\theta) = \frac{2}{3} \left\langle \left| \boldsymbol{\mu} : \boldsymbol{\sigma}^{(0)}(\theta) \right|^{n+1} \right\rangle_{\mathcal{S}}^{\frac{1}{n+1}} \tag{E.9}$$

Thus, in the limit $K \to +\infty$, the pristine single crystal becomes an isotropic material of Lode angle-dependent potential. Using the analytical form Eq. E.7, it can be shown that $g_n\left(\frac{\pi}{3}\right) = g_n(0)$, $g_n'(0) = g_n'\left(\frac{\pi}{3}\right) = 0$ and $g_n(\theta) + g_n''(\theta) \geq 0$, which will be useful in what follows. Note that in the limit in which $n \to +\infty$, the single crystal becomes a perfectly plastic Tresca material, as already pointed out by other studies (Cailletaud, 2009; Mbiakop et al., 2016), which means that:

$$g_\infty(\theta) \propto \frac{1}{\cos\left(\theta - \frac{\pi}{6} - \left\lfloor \frac{3\theta}{\pi} \right\rfloor \frac{\pi}{3}\right)} \tag{E.10}$$

Functions $g_1$ and and $g_\infty$ are plotted in Fig. E.19; all other $g_n$ for odd $n$ lie in between in a continuum from $g_1$ to $g_\infty$ as $n$ increases.

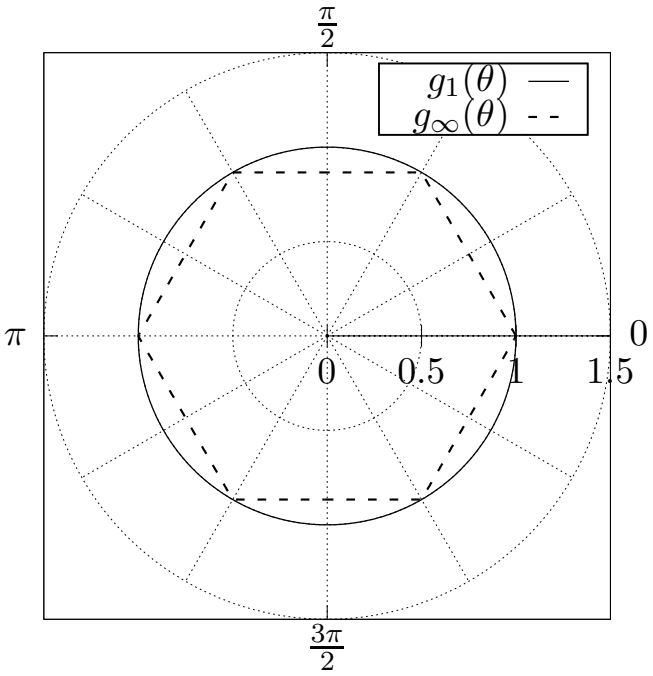


Figure E.19: Polar plot of normalized functions $g_n(\theta)/g_n(0)$ where $\theta$ is the angular coordinate. This representation corresponds to the $\pi$-plane of gauge surfaces.

*Appendix E.2. Hollow sphere under hydrostatic loading*

It is recalled that Benallal (2018) demonstrated that a hollow sphere with an isotropic perfect-plastic matrix following a yield function expressed as:

$$\mathcal{F}(\boldsymbol{\sigma}) = \left[ \frac{\sigma_{\mathrm{eq}}^{\mathrm{vM}}}{\sigma^c} g(\theta) \right]^2 - 1 \tag{E.11}$$

with $g$ a smooth function verifying $g(\theta) + g''(\theta) \geq 0$ and subjected to pure hydrostatic tension has the same yield strength as a hollow sphere made of a perfectly plastic von Mises material of uniaxial tension yield limit $\sigma^0$:

$$\sigma^0 = \frac{1}{\sqrt{g\left(\frac{\pi}{3}\right)^2 + g'\left(\frac{\pi}{3}\right)^2}}\sigma^{\mathrm{c}} \tag{E.12}$$

while under pure hydrostatic compression, this result becomes:

$$\sigma^0 = \frac{1}{\sqrt{g\,(0)^2 + g'\,(0)^2}}\sigma^{\mathrm{c}} \tag{E.13}$$

Mbiakop et al. (2015a) made the (unstated) hypothesis that a similar equivalence was true for viscoplastic materials. If such a result is at least approximately verified, Eqs. E.12 and E.13 can be used with $g_n$ instead of $g$. Since $g_n$ is $\frac{\pi}{3}$-periodic, Eqs. E.12 and E.13 are identical. This means that a hollow sphere of viscoplastic single crystal with $K \to +\infty$ would then have the same plastic potential under pure hydrostatic loading as a hollow sphere of viscoplastic von Mises material of parameters $(\dot{\varepsilon}_0, \sigma_0) = (\dot{\gamma}_0, \sigma^{\mathrm{c}}/g_n(0))$ in the case where $n$ is finite (in the case $n = +\infty$, Tresca yield function is not smooth).

On the one hand, the plastic potential of a hollow sphere in a viscoplastic von Mises matrix of reference stress $\sigma^{\mathrm{c}}$ subjected to hydrostatic loading, as found in Leblond et al. (1994), writes:

$$U(\Sigma_{\mathrm{m}}) = \frac{\dot{\gamma}_0}{n+1}\frac{(a g_n(0)\Sigma_{\mathrm{m}})^{n+1}}{\left[\sigma^{\mathrm{c}}\, n\left(f^{-\frac{1}{n}} - 1\right)\right]^n} \quad \text{with} \quad a = \frac{3}{2} \text{ (spherical void)} \tag{E.14}$$

On the other hand, when $\tau_s^{\mathrm{c}} = K^{1/n}\sigma^c$ and $K \to +\infty$, Eq. 35 becomes:

$$U(\Sigma_{\mathrm{m}}) = \frac{\dot{\gamma}_0}{n+1}\frac{(q_{\mathrm{J}}\Sigma_{\mathrm{m}})^{n+1}}{\left[\sigma^{\mathrm{c}}\,(1-f)\right]^n}\left(\sqrt{\lim_{K\to+\infty}\left[(1-f)\frac{(\tau^{\mathrm{c}})^2}{K}\boldsymbol{I} : \overline{\mathbb{S}} : \boldsymbol{I}\right]}\right)^{n+1} \tag{E.15}$$

Thus, using the hollow sphere equivalence discussed previously, Eq. E.14 and Eq. E.15 can be equated. However, before proceeding, the quantity $\boldsymbol{I} : \left(\overline{\mathbb{S}}/K\right) : \boldsymbol{I}$ of Eq. E.15 should be evaluated in the limit $K \to +\infty$. First, according to Böhlke and Bertram (2001), the pseudo-compliance tensor of a pristine crystal with infinite equiangular slip systems[8] becomes isotropic:

$$\frac{(\tau^{\mathrm{c}})^2}{K}\mathbb{S}_i \underset{K\to+\infty}{\longrightarrow} \mathbb{S}_{\mathrm{iso}} \quad \text{with} \quad \mathbb{S}_{\mathrm{iso}} = \frac{1}{3\kappa}\mathbb{J} + \frac{1}{2\mu_0}\mathbb{K} \quad \text{where} \quad \mu_0 = 5 \tag{E.16}$$

Then, following Nemat-Nasser et al. (1993), $\mathbb{A}$ associated with an isotropic matrix is such that:

$$\begin{aligned}\frac{1}{\mu}\left[\mathbb{A}\left(\underset{\sim}{\xi}, \frac{1}{3\kappa}\mathbb{J} + \frac{1}{2\mu}\mathbb{K}\right)\right]_{ijkl} &= \delta_{ik}\delta_{jl} + \delta_{il}\delta_{jk} - \frac{1}{\xi^2}(\delta_{ik}\xi_j\xi_l + \delta_{il}\xi_j\xi_k + \delta_{jk}\xi_i\xi_l + \delta_{jl}\xi_i\xi_k) \\ &+ \frac{6\kappa - 4\mu}{3\kappa + 4\mu}\left[\delta_{ij}\delta_{kl} - \frac{1}{\xi^2}(\delta_{ij}\xi_k\xi_l + \delta_{kl}\xi_i\xi_j)\right] + \frac{4}{\xi^4}\frac{3\kappa + \mu}{3\kappa + 4\mu}\xi_i\xi_j\xi_k\xi_l\end{aligned} \tag{E.17}$$

which yields, in the case of a random distribution of spherical voids:

$$\left\langle \mathbb{A}\left(\frac{1}{3\kappa}\mathbb{J} + \frac{1}{2\mu}\mathbb{K}\right)\right\rangle_{\Omega_0} = \frac{12\kappa\mu}{3\kappa + 4\mu}\mathbb{J} + h(\kappa, \mu)\mathbb{K} \tag{E.18}$$

where $h$ is a coefficient depending on $\kappa$ and $\mu$ that do not need to be detailed here. Alternatively, if the voids are distributed periodically with a cubic unit-cell, Eq. E.17 provides the following result:

$$\mathbb{A}_{00}\left(\frac{1}{3\kappa}\mathbb{J} + \frac{1}{2\mu}\mathbb{K}\right) = \frac{12\kappa\mu}{3\kappa + 4\mu}\left(\sum_{\underset{\sim}{\xi}}\left|g_0\left(\underset{\sim}{\xi}\right)\right|^2\right)\mathbb{J} + h'(\kappa, \mu)\mathbb{K}' + h''(\kappa, \mu)\mathbb{K}'' \quad \text{with} \quad \sum_{\underset{\sim}{\xi}}\left|g_0\left(\underset{\sim}{\xi}\right)\right|^2 = \frac{1-f}{f} \tag{E.19}$$

with $h'$ and $h''$ are coefficients depending on $\kappa$ and $\mu$ and where the last equality is obtained using three-dimensional Parseval identity. Note that the factor $f/(1-f)$, whose absence may have surprised in Eq. 31, is recovered as a normalization factor. Finally, considering Eq. E.18 (respectively Eq. E.19) in the limit $(\kappa, \mu) \to (+\infty, 5)$ and injecting it in Eq. 32 (respectively Eq. 31) that defines $\overline{\mathbb{S}}$ brings:

$$\frac{(\tau^{\mathrm{c}})^2}{K}\boldsymbol{I} : \overline{\mathbb{S}} : \boldsymbol{I} \underset{K\to+\infty}{\longrightarrow} \frac{3}{20}\frac{f}{1-f} \tag{E.20}$$

Equating Eq. E.14 and Eq. E.15 thus leads to:

$$q_{\mathrm{J}} = a\, g_n(0)\sqrt{\frac{20}{3f}}\left(\frac{1-f}{n(f^{-1/n} - 1)}\right)^{\frac{n}{n+1}} \tag{E.21}$$

which is the condition on $q_{\mathrm{J}}$ that is necessary to recover the exact potential in the limit $K \to +\infty$. Note that this result does not depend on the number of crystals in the matrix (since they all become the same isotropic material in the limit $K \to +\infty$) nor on the distribution of cavities — *i.e.* random or with cubic periodicity.

[8] Remember that in the limit $K \to +\infty$, $(\tau^{\mathrm{c}})^2\,\mathbb{S}_i$ goes to infinity and needs renormalization by $K$ to yield a finite value.

## References


Arminjon, M., 1991. A regular form of the Schmid law. Application to the ambiguity problem. Textures and Microstructures 14-18, 1121–1128.

Barrioz, P., Hure, J., Tanguy, B., 2019. Effect of dislocation channelling on void growth to coalescence in FCC crystals. Materials Science and Engineering: A 749, 255–270.

Barrioz, P.O., 2019. Rupture ductile des matériaux CFC irradiés. Ph.D. thesis. Université Paris-Saclay.

Becker, R., Needleman, A., Suresh, S., Tvergaard, V., Vasudevan, A., 1989. An analysis of ductile failure by grain boundary void growth. Acta Metallurgica 37, 99–120.

Benallal, A., 2018. On some features of the effective behaviour of porous solids with J2- and J3-dependent yielding matrix behaviour. Comptes Rendus Mécanique 346, 77–88.

Benallal, A., Desmorat, R., Fournage, M., 2014. An assessment of the role of the third stress invariant in the Gurson approach for ductile fracture. European Journal of Mechanics - A/Solids 47, 400–414.

Benzerga, A., Besson, J., 2001. Plastic potentials for anisotropic porous solids. European Journal of Mechanics - A/Solids 20, 397–434.

Benzerga, A.A., Leblond, J.B., 2010. Ductile fracture by void growth to coalescence. Advances in Applied Mechanics 44, 169–305.

Besson, J., 2010. Continuum models of ductile fracture: A review. International Journal of Damage Mechanics 19, 3–52.

Böhlke, T., Bertram, A., 2001. Isotropic orientation distributions of cubic crystals. Journal of the Mechanics and Physics of Solids 49, 2459–2470.

Cadet, C., Besson, J., Flouriot, S., Forest, S., Kerfriden, P., Lacourt, L., de Rancourt, V., 2022. Strain localization analysis in materials containing randomly distributed voids: Competition between extension and shear failure modes. Journal of the Mechanics and Physics of Solids 166, 104933.

Cadet, C., Besson, J., Flouriot, S., Forest, S., Kerfriden, P., de Rancourt, V., 2021. Ductile fracture of materials with randomly distributed voids. International Journal of Fracture 230, 193 – 223.

Cailletaud, G., 2009. An overview of the anatomy of crystal plasticity models. Advanced Engineering Materials 11, 710–716.

Castañeda, P.P., Suquet, P., 1997. Nonlinear composites. Advances in Applied Mechanics 34, 171–302.

Cazacu, O., Revil-Baudard, B., Lebensohn, R.A., Gărăjeu, M., 2013. On the combined effect of pressure and third invariant on yielding of porous solids with von Mises matrix. Journal of Applied Mechanics 80.

CEA, 2022. AMITEX FFTP. amitexfftp.github.io/AMITEX/index.html .

Chabaud-Reytier, M., Allais, L., Caes, C., Dubuisson, P., Pineau, A., 2003. Mechanisms of stress relief cracking in titanium stabilised austenitic stainless steel. Journal of Nuclear Materials 323, 123–137.

Chang, L., Sun, W., Cui, Y., Zhang, F., Yang, R., 2014. Effect of heat treatment on microstructure and mechanical properties of the hot-isostatic-pressed Inconel 718 powder compact. Journal of Alloys and Compounds 590, 227–232.

Cheng, L., Monchiet, V., Morin, L., de Saxcé, G., Kondo, D., 2015. An analytical Lode angle dependent damage model for ductile porous materials. Engineering Fracture Mechanics 149, 119–133.

Chouksey, M., Keralavarma, S.M., Basu, S., 2019. Computational investigation into the role of localisation on yield of a porous ductile solid. Journal of the Mechanics and Physics of Solids 130, 141–164.

Dakshinamurthy, M., Kowalczyk-Gajewska, K., G., V., 2021. Influence of cristallographic orientation on the void growth at the grain boundary in bi-crystals. International Journal of Solids and Structures 212, 61–79.

Danas, K., Castañeda, P.P., 2009. A finite-strain model for anisotropic viscoplastic porous media: Part I - Theory. European Journal of Mechanics-A/Solids 28, 387–401.

Danas, K., Idiart, M., Castañeda, P.P., 2008. A homogenization-based constitutive model for isotropic viscoplastic porous media. International Journal of Solids and Structures 45, 3392–3409.

Danas, K., Ponte Castañeda, P., 2012. Influence of the Lode parameter and the stress triaxiality on the failure of elasto-plastic porous materials. International Journal of Solids and Structures 49, 1325–1342.

Decreus, B., Deschamps, A., Donnadieu, P., Ehrström, J., 2013. On the role of microstructure in governing fracture behavior of an aluminum–copper–lithium alloy. Materials Science and Engineering: A 586, 418–427.

Demkowicz, M.J., 2020. A threshold density of helium bubbles induces a ductile-to-brittle transition at a grain boundary in nickel. Journal of Nuclear Materials 533.

Deshpande, N.U., Gokhale, A., Denzer, D.K., Liu, J., 1998. Relationship between fracture toughness, fracture path, and microstructure of 7050 aluminum alloy: Part I - Quantitative characterization. Metallurgical and Materials Transactions A 29, 1191–1201.

Dormieux, L., Kondo, D., 2010. An extension of Gurson model incorporating interface stresses effects. Int. J. Eng. Sci. 48, 575–581.

Foltz, J.W., Welk, B., Collins, P.C., Fraser, H.L., Williams, J.C., 2011. Formation of grain boundary $\alpha$ in $\beta$ Ti alloys: Its role in deformation and fracture behavior of these alloys. Metallurgical and Materials Transactions A 42, 645–650.

Fourmeau, M., Marioara, C., Børvik, T., Benallal, A., Hopperstad, O., 2015. A study of the influence of precipitate-free zones on the strain localization and failure of the aluminium alloy AA7075-T651. Philosophical Magazine 95, 3278–3304.

Francfort, G., Murat, F., 1986. Homogenization and optimal bounds in linear elasticity. Archive for Rational Mechanics and Analysis 94, 307–334.

Fritzen, F., Forest, S., Böhlke, T., Kondo, D., Kanit, T., 2012. Computational homogenization of elasto-plastic porous metals. International Journal of Plasticity 29, 102–119.

Fu, J., Zhang, Y., 2020. Mechanism of crack initiation and propagation of 316LN stainless steel during the high temperature tensile deformation. Materials Research Express 7.

Gambin, V., 1991. Crystal plasticity based on yield surfaces with rounded-off corners. Zeitschrift für Angewandte Mathematik und Mechanik 71, 265–268.

Gologanu, M., Leblond, J.B., Devaux, J., 2001. Theoretical models for void coalescence in porous ductile solids. ii. coalescence "in columns". International Journal of Solids and Structures 38, 5595–5604.

Gräf, M., Hornbogen, E., 1977. Observation of ductile intercrystalline fracture of an Al-Zn-Mg alloy. Acta Metallurgica 25, 883–889.

Gurson, A., 1977. Continuum theory of ductile rupture by void nucleation and growth: Part I - Yield criteria and flow rules for porous ductile media. Journal of Engineering Materials and Technology 99, 2–15.

Han, X., Besson, J., Forest, S., Tanguy, B., Bugat, S., 2013. A yield function for single crystals containing voids. International Journal of Solids and Structures 50, 2115–2131.

Hashin, Z., Shtrikman, S., 1963. A variational approach to the theory of the elastic behaviour of multiphase materials. Journal of the Mechanics and Physics of Solids 11, 127–140.

Hill, R., 1948. A theory of the yielding and plastic flow of anisotropic metals. Proc. R. Soc. Lond. A 193, 281–297.

Hill, R., 1972. Continuum Mechanics and Related Problems of Analysis (Muskhelishvili 80th Anniversary Volume). chapter An invariant treatment of interfacial discontinuities in elastic composites. pp. 597–604.

Hoff, N.J., 1954. Approximate analysis of structures in the presence of moderately large creep deformations. Quarterly of Applied Mathematics 12, 49–55.

Hojná, A., 2017. Overview of intergranular fracture of neutron irradiated austenitic stainless steels. Metals 7, 392.

Hornbogen, E., Kreye, H., 1982. The mechanism of pseudo-intercrystalline brittleness of precipitation-hardened alloys and tempered steels. Journal of Materials Science 17, 979–988.

Hure, J., 2019. A coalescence criterion for porous single crystals. Journal of the Mechanics and Physics of Solids 124, 505–525.

Hure, J., 2021. Yield criterion and finite strain behavior of random porous isotropic materials. European Journal of Mechanics - A/Solids 85, 104143.

Hutchinson, J.W., 1976. Bounds and self-consistent estimates for creep of polycrystalline materials. Proceedings of the Royal Society of London A 348, 101–127.

Jeong, W., Lee, C., Moon, J., Jang, D., Lee, M.G., 2018. Grain scale reprensentative volume element simulation to investigate the effect of crystal orientation on void growth in single and multi-crystals. Metals 8, 436.
Judge, C.D., Gauquelin, N., Walters, L., Wright, M., Cole, J.I., Madden, J., Botton, G.A., Griffiths, M., 2015. Intergranular fracture in irradiated Inconel X-750 containing very high concentrations of helium and hydrogen. Journal of Nuclear Materials 457, 165–172.
Judge, C.D., Griffiths, M., Waters, L., Wright, M., Bickel, G., Woo, O., Stewart, M., Douglas, S., 2012. Embrittlement of nickel alloys in a CANDU reactor environment. Effects of Radiation on Nuclear Materials 25.
Kassner, M., Hayes, T., 2003. Creep cavitation in metals. International Journal of Plasticity 19, 1715–1748.
Kawabata, T., Izumi, O., 1976. Ductile fracture in the interior of precipitate free zone in an Al-6.0%Zn-2.6%Mg alloy. Acta Metallurgica 24, 817–825.
Keralavarma, S., Reddi, D., Benzerga, A., 2020. Ductile failure as a constitutive instability in porous plastic solids. Journal of the Mechanics and Physics of Solids 139, 103917.
Keralavarma, S.M., 2017. A multi-surface plasticity model for ductile fracture simulations. Journal of the Mechanics and Physics of Solids 103, 100–120.
Keralavarma, S.M., Benzerga, A.A., 2010. A constitutive model for plastically anisotropic solids with non-spherical voids. Journal of the Mechanics and Physics of Solids 58, 874–901.
Khavasad, P.H., Keralavarma, S.M., 2021. Effective yield criterion for a porous single crystal accounting for void size effects. Mechanics of Materials 160, 103950.
Koplik, J., Needleman, A., 1988. Void growth and coalescence in porous plastic solids. International Journal of Solids and Structures 24, 835–853.
Kuramoto, S., Itoh, G., Kanno, M., 1996. Intergranular fracture in some precipitation-hardened aluminum alloys at low temperatures. Metallurgical and Materials Transactions A 27A, 3081–3088.
Lebensohn, R., Idiart, M., Castañeda, P.P., Vincent, P.G., 2011. Dilatational viscoplasticity of polycrystalline solids with intergranular cavities. Philosophical Magazine 91, 3038–3067.
Leblond, J., Perrin, G., Suquet, P., 1994. Exact results and approximate models for porous viscoplastic solids. International Journal of Plasticity 10, 213–235.
Leblond, J.B., Kondo, D., Morin, L., Remmal, A., 2018. Classical and sequential limit analysis revisited. Comptes Rendus Mécanique 346, 336–349.
Leblond, J.B., Morin, L., 2014. Gurson's criterion and its derivation revisited. Journal of Applied Mechanics 81, 51012.
Li, H., Li, J., Tang, B., Fan, J., Yuan, H., 2017. Simulation of intergranular ductile cracking in $\beta$ titanium alloys based on a micro-mechanical damage model. Materials 10.
Li, S.W., Wen, Z.X., Yue, Z.F., Gao, J., 2015. Creep behavior and life assessment of anisotropic bicrystals with a void and without void in different kinds of grain boundaries. Materialwissenschaft und Werkstofftechnik 46, 1169–1176.
Lin, Y., Li, L., He, D.G., Chen, M.S., Liu, G.Q., 2017. Effects of pre-treatments on mechanical properties and fracture mechanism of a nickel-based superalloy. Materials Science and Engineering: A 679, 401–409.
Ling, C., Besson, J., Forest, S., Tanguy, B., Latourte, F., Bosso, E., 2016. An elastoviscoplastic model for porous single crystals at finite strains and its assessment based on unit cell simulations. International Journal of Plasticity 84, 58–87.
Liu, W., Huang, H., Tang, J., 2010. FEM simulation of void coalescence in FCC crystals. Computational Materials Science 50, 411–418.
Liu, W., Zhang, X., Tang, J., 2009. Study on the growth behavior of voids located at the grain boundary. Mechanics of Materials 41, 799–809.
Lynch, S.P., 1991. Mechanisms of intergranular fracture, in: Grain Boundary Chemistry and Intergranular Fracture, Trans Tech Publications Ltd. pp. 1–24.
Lynch, S.P., Muddle, B.C., Pasang, T., 2002. Mechanisms of brittle intergranular fracture in Al-Li alloys and comparison with other alloys. Philosophical Magazine A 82, 3361–3373.
Madou, K., Leblond, J.B., 2012. A gurson-type criterion for porous ductile solids containing arbitrary ellipsoidal voids—ii: Determination of yield criterion parameters. Journal of the Mechanics and Physics of Solids 60, 1037–1058.
Mbiakop, A., Constantinescu, A., Danas, K., 2015a. An analytical model for porous single cristals with ellipsoidal voids. Journal of the Mechanics and Physics of Solids 84, 436–467.
Mbiakop, A., Constantinescu, A., Danas, K., 2015b. A model for porous single crystals with cylindrical voids of elliptical cross-section. International Journal of Solids and Structures 64-65, 100–119.
Mbiakop, A., Danas, K., Constantinescu, A., 2016. A homogenization based yield criterion for a porous Tresca material with ellipsoidal voids. International Journal of Fracture 200, 209–225.
Mills, W., 1980. The deformation and fracture characteristics of Inconel X-750 at room temperature and elevated temperatures. Metallurgical Transactions A 11, 1039–1047.
Miura, T., Fujii, K., Fukuya, K., 2015. Micro-mechanical investigation for effects of helium on grain boundary fracture of austenitic steel. Journal of Nuclear Materials 457, 279–290.
Molkeri, A., Srivastava, A., Osovski, S., Needleman, A., 2020. Influence of Grain Size Distribution on Ductile Intergranular Crack Growth Resistance. Journal of Applied Mechanics 87.
Monchiet, V., Cazacu, O., Charkaluk, E., Kondo, D., 2008. Macroscopic yield criteria for plastic anisotropic materials containing spheroidal voids. International Journal of Plasticity 24, 1158–1189.
Morin, L., 2012. Influence de l'effet de forme et de taille des cavités, et de l'anisotropie plastique sur la rupture ductile. Ph.D. thesis. Université Pierre et Marie Curie.
Morin, L., Leblond, J.B., Kondo, D., 2015. A Gurson-type criterion for plastically anisotropic solids containing arbitrary ellipsoidal voids. International Journal of Solids and Structures 77, 86–101.
Naimark, M., 1964. Linear Representations of the Lorentz Group.
Nelder, J.A., Mead, R., 1965. A simplex method for function minimization. Comput. J. 7, 308–313.
Nemat-Nasser, S., Yu, N., Hori, M., 1993. Bounds and estimates of overall moduli of composites with periodic microstructure. Mechanics of Materials 15, 163–181.
Nervi, J., Idiart, M., 2015. Bounding the plastic strength of polycrystalline voided solids by linear-comparison homogenization techniques. Proceedings of the Royal Society A: Mathematical, Physical and Engineering Sciences 471, 20150380–20150380.
Norris, A.N., 1990. The Effective Moduli of Layered Media— A New Look at an Old Problem. Springer New York, New York, NY. pp. 321–339.
Osovski, S., Srivastava, A., Williams, J., Needleman, A., 2015. Grain boundary crack growth in metastable titanium $\beta$ alloys. Acta Materialia 82, 167–178.
Pardoen, T., Dumont, D., Deschamps, A., Bréchet, Y., 2003. Grain boundary versus transgranular ductile failure. Journal Of The Mechanics And Physics Of Solids 51, 637–665.
Pardoen, T., Scheyvaerts, F., Simar, A., Tekoğlu, C., Onck, P.R., 2010. Multiscale modeling of ductile failure in metallic alloys. Comptes Rendus Physique 11, 326–345. Computational metallurgy and scale transitions.
Pasang, T., Symonds, N., Moutsos, S., Wanhill, R., Lynch, S., 2012. Low-energy intergranular fracture in al–li alloys. Engineering Failure Analysis 22, 166–178.
Paux, J., Brenner, R., Kondo, D., 2018. Plastic yield criterion and hardening of porous single crystals. International Journal of Solids and Structures 132-133, 80–95.
Paux, J., Morin, L., Brenner, R., Kondo, D., 2015. An approximate yield criterion for porous single crystals. European Journal of Mechanics A/Solids 51, 1–10.
Pavinich, W., Raj, R., 1977. Fracture at elevated temperature. Metallurgical Transactions A 8, 1917–1933.
Pineau, A., Benzerga, A., Pardoen, T., 2016. Failure of metals: Part I - Brittle and ductile fracture. Acta Materiala 107, 424–483.
Plateau, J., Henry, G., Crussard, C., 1957. Quelques nouvelles applications de la microfractographie. Revue de métallurgie 54, 200–216.

Pommier, H., Busso, E.P., Morgeneyer, T.F., Pineau, A., 2016. Intergranular damage during stress relaxation in AISI 316L-type austenitic stainless steels: Effect of carbon, nitrogen and phosphorus contents. Acta Materialia 103, 893–908.
Poole, W., Wang, X., Embury, J., Lloyd, D., 2019. The effect of manganese on the microstructure and tensile response of an al-mg-si alloy. Materials Science and Engineering: A 755, 307–317.
Rice, J., 1976. The localization of plastic deformation, pp. 207–220.
Rice, J.R., Tracey, D.M., 1969. On the ductile enlargement of voids in triaxial stress fields. Journal of the Mechanics and Physics of Solids 17, 201–217.
Riedel, H., 1987. Fracture at high temperatures. Springer Verlag.
Ringdalen, I.G., Jensen, I.J.T., Marioara, C.D., Friis, J., 2021. The role of grain boundary precipitates during intergranular fracture in 6xxx series aluminium alloys. Metals 11.
Schulz, B., McMahon, C., 1973. Fracture of alloy steels by intergranular microvoid coalescence as influenced by composition and heat treatment. Metallurgical Transactions 4, 2485–2489.
Song, D., Ponte-Castañeda, P., 2017a. A finite-strain homogenization model for viscoplastic porous single crystals: Part I - Theory. Journal of the Mechanics and Physics of Solids 107, 560–579.
Song, D., Ponte-Castañeda, P., 2017b. A finite-strain homogenization model for viscoplastic porous single crystals: Part II - Applications. Journal of the Mechanics and Physics of Solids 107, 580–602.
Song, D., Ponte Castañeda, P., 2018. A multi-scale homogenization model for fine-grained porous viscoplastic polycrystals: I – Finite-strain theory. Journal of the Mechanics and Physics of Solids 115, 102–122.
Suquet, P., 1982. Plasticité et homogénéisation. Ph.D. thesis. Université Pierre et Marie Curie.
Suresh, S., Vasudevan, A., Tosten, M., Howell, P., 1987. Microscopic and macroscopic aspects of fracture in lithium-containing aluminum alloys. Acta Metallurgica 35, 25–46.
Sénac, C., Scherer, J.M., Hure, J., Helfer, T., Tanguy, B., 2022. Homogenized constitutive equations for porous single crystals plasticity. European Journal of Mechanics - A/Solids , 104642.
Thomas, G., Nutting, J., 1957. The plastic deformation of aged aluminum alloys. Journal of the Institute of Metals 86, 7–14.
Thomas, G., Nutting, J., 1959. The ageing characteristics of aluminum alloys. Journal of the Institute of Metals 88, 81–90.
Thomason, P.F., 1985. Three-dimensional models for the plastic limit-loads at incipient failure of the intervoid matrix in ductile porous solids. Acta Metallurgica 33, 1079–1085.
Torki, M., Keralavarma, S., Benzerga, A., 2021. An analysis of Lode effects in ductile failure. Journal of the Mechanics and Physics of Solids 153, 104468.
Torquato, S., 1991. Random heterogeneous media: microstructure and improved bounds on effective properties. Appl. Mech. Rev. 44, 37–76.
Tsun, K., 1953. The overheating and burning of steel, in: Symposium on Industrial Failure of Engineering Metals and Alloys, pp. 95–104.
Tvergaard, V., 1982. On localization in ductile materials containing spherical voids. Int J Fract 18, 237–=252.
Unwin, P.T., Smith, G.C., 1969. The microstructure and mechanical properties of Al-6% Zn-3% Mg. Journal of the Institute of Metals 97, 299–310.
Varley, P., Day, M., Sendorek, A., 1957. Unknown. Journal of the Institute of Metals 86, 337–351.
Vasudévan, A.K., Doherty, R.D., 1987. Grain boundary ductile fracture in precipitation hardened aluminium alloys. Acta Metallica 35, 1193–1219.
Venkiteswaran, P.K., Taplin, D.M.R., 1974. The creep fracture of Inconel X-750 at 700°C. Metal Science 8, 97–106.
Vincent, P.G., Suquet, P., Monerie, Y., Moulinec, H., 2014. Effective flow surface of porous materials with two populations of voids under internal pressure: II - Full-field simulations. International Journal of Plasticity 56, 74–98.
Vishwakarma, V., Keralavarma, S., 2019. Micromechanical modeling and simulation of the loading path dependence of ductile failure by void growth and coalescence. International Journal of Solids and Structures 166, 135–153.
Walpole, L., 1981. Elastic behavior of composite materials: Theoretical foundations. Advances in Applied Mechanics 21, 169–242.
Wen, Z.X., Yue, Z.F., 2007. On the crystallographic study of growth characterization of isolated void in the grain boundary. Computational Materials Science 40, 140–146.
Willis, J., 1977. Bounds and self-consistent estimates for the overall properties of anisotropic composites. Journal of the Mechanics and Physics of Solids 25, 185–202.
Wojtacki, K., Vincent, P.G., Suquet, P., Moulinec, H., Boittin, G., 2020. A micromechanical model for the secondary creep of elasto-viscoplastic porous materials with two rate-sensitivity exponents: Application to a mixed oxide fuel. International Journal of Solids and Structures 184, 99–113.
Zaefferer, S., Kuo, J.C., Zhao, Z., Winning, M., Raabe, D., 2003. On the influence of the grain boundary misorientation on the plastic deformation of aluminum bicrystals. Acta Materialia 51, 4719–4735.
Zhang, X.M., Liu, W.H., Tang, J., Ye, L.Y., 2008. Influence of crystallographic orientation on growth behavior of spherical voids. Journal of Central South University of Technology 15, 159–164.
Zheng, K.Y., Dong, J., Zeng, X.Q., Ding, W.J., 2008. Effect of precipitation aging on the fracture behavior of Mg–11Gd–2Nd–0.4Zr cast alloy. Materials Characterization 59, 857–862.